

AD/

ESD-TR-85-241

Quarterly Technical Report

Solid State Research

1985:3

Lincoln Laboratory

MASSACHUSETTS INSTITUTE OF TECHNOLOGY

LEXINGTON, MASSACHUSETTS



Prepared under Electronic Systems Division Contract F19628-85-C-0002.

Approved for public release; distribution unlimited.

ADA168053

The work reported in this document was performed at Lincoln Laboratory, a center for research operated by Massachusetts Institute of Technology, with the support of the Department of the Air Force under Contract F19628-85-C-0002.

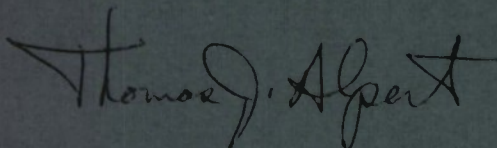
This report may be reproduced to satisfy needs of U.S. Government agencies.

The views and conclusions contained in this document are those of the contractor and should not be interpreted as necessarily representing the official policies, either expressed or implied, of the United States Government.

The ESD Public Affairs Office has reviewed this report, and it is releasable to the National Technical Information Service, where it will be available to the general public, including foreign nationals.

This technical report has been reviewed and is approved for publication.

FOR THE COMMANDER

A handwritten signature in dark ink, appearing to read "Thomas J. Alpert". The signature is fluid and cursive, with the first name "Thomas" and last name "Alpert" clearly legible.

Thomas J. Alpert, Major, USAF
Chief, ESD Lincoln Laboratory Project Office

Non-Lincoln Recipients

PLEASE DO NOT RETURN

Permission is given to destroy this document
when it is no longer needed.

**MASSACHUSETTS INSTITUTE OF TECHNOLOGY
LINCOLN LABORATORY**

SOLID STATE RESEARCH

QUARTERLY TECHNICAL REPORT

1 MAY — 31 JULY 1985

ISSUED 8 NOVEMBER 1985

Approved for public release; distribution unlimited.

LEXINGTON

MASSACHUSETTS

ABSTRACT

This report covers in detail the solid state research work of the Solid State Division at Lincoln Laboratory for the period 1 May through 31 July 1985. The topics covered are Solid State Device Research, Quantum Electronics, Materials Research, Microelectronics, and Analog Device Technology. Funding is primarily provided by the Air Force, with additional support provided by the Army, DARPA, Navy, SDIO, NASA, and DOE.

TABLE OF CONTENTS

Abstract	iii
List of Illustrations	viii
List of Tables	ix
Introduction	xi
Reports on Solid State Research	xiii
Organization	xxi
 1. SOLID STATE DEVICE RESEARCH	 1
1.1 Double-Heterostructure InGaAs/InP PIN Photodetectors	1
 2. QUANTUM ELECTRONICS	 9
2.1 Er:YAG Laser Crystal Characterization	9
2.2 KTP Frequency Conversion	10
 3. MATERIALS RESEARCH	 13
3.1 CMOS Gate Arrays and Dynamic Shift Registers Fabricated in Zone-Melting-Recrystallized SOI Films	13
3.2 Optical and Electrical Properties of V-Doped InP	17
 4. MICROELECTRONICS	 21
4.1 S-Band Modeling of a Planar Millimeter-Wave Receptor	21
4.2 Reproducible Microwave Performance of GaAs Permeable Base Transistors	23
4.3 Spectral Measurement of Quantum Well Width	26
 5. ANALOG DEVICE TECHNOLOGY	 29
5.1 Thin Stripline Dielectrics with Passivated Superconductors	29
5.2 Bulk-Acoustic-Wave Reflections from Optically Generated Holographic Gratings	32
5.3 Edge Detection by Convolution with a Gaussian Screen	35
5.4 Fast Wideband Phase-Locked Loop for Narrowband Excision	38

LIST OF ILLUSTRATIONS

Figure No.		Page
1-1	Inverted-Mesa Double-Heterostructure PIN Photodetector. The InGaAs Layer Thickness d Was 1.5 to 5 μm and Its Carrier Concentration Was Either (a) $6 \times 10^{14} \text{ cm}^{-3} < n^- < 1 \times 10^{16} \text{ cm}^{-3}$, or (b) $n = p = 1 \times 10^{12} \text{ cm}^{-3}$. Device Diameters D Ranged from 6 to 75 μm .	1
1-2	Calculated Curves Showing Factors Which Are Important in Design of High-Speed PIN Photodetectors. (a) RC Time Constant, for Two Device Diameters D , and Transit Time vs Depletion Depth. (b) Depletion Depth at Breakdown for Various Carrier Concentrations.	2
1-3	Photograph of Detector Package. The Device Chip Is Mounted (Inset) on the 50- Ω Alumina Microstrip Carrier (White Square at Center) Such That Both Front- and Back-Illumination Are Possible.	4
1-4	InGaAs Carrier Concentration vs Distance from pn Junction for n-InGaAs Double-Heterostructure Device. The Width of the n^+n Interface and the Final Value of the Carrier Concentration Are Limited by the CV Probing Method Used.	4
1-5	Capacitance vs Voltage for SI-InGaAs Double-Heterostructure Device Near $V = 0$. The Lack of Variation with Reverse Voltage Indicates that the InGaAs Layer Is Fully Depleted at $V = -0.5 \text{ V}$.	5
1-6	Current vs Reverse-Voltage Characteristics for n-InGaAs Device in the Dark and Under Front-Illumination. The Dark Current Shows the Generation and Tunneling (Exponential) Regimes. The Voltage Independence of the Photocurrent Is a Result of Long Diffusion Lengths Relative to the Layer Thickness.	6
1-7	Response of Front-Illuminated SI-InGaAs Detector to Comb-Generator-Driven InGaAsP Laser. System-Limited FWHM Is 52 ps.	7
1-8	Response of Back-Illuminated n-InGaAs Device to 10-GHz Output of Intracavity-Loss Modulator Laser	7
2-1	Spectroscopy of Er:YAG	9
3-1	Photograph of a 3-in.-dia. SOI Wafer After Fabrication of CMOS Test Chips	14
3-2	(a) Photograph of an SOI CMOS Gate-Array Circuit. (b) Output Waveforms of SOI Ring Oscillators with Fanout of 1 or 3. (c) Ring Oscillator Stage Delay as a Function of Supply Voltage for SOI, SOS, and Bulk Si Gate-Array Circuits.	15

3-3	(a) Photograph of an SOI CMOS Dynamic Shift Register. (b) Input and Output Waveforms of the Shift Register at a Clock Frequency of 10 MHz.	15
3-4	Optical Absorption vs Wavelength for an n-Type InP Sample Doped with V, but Not Intentionally Doped with Any Other Impurity	16
3-5	Optical Absorption vs Wavelength for Regions of a Zn-Doped, p-Type InP Crystal Grown Before and After Addition of V to the Melt	18
3-6	Carrier Concentration vs Distance Along the Vertical Axis for an n-Type InP Crystal Initially Grown Without Intentional Doping, and Then Doped with V	19
4-1	Smith Chart Display of Impedance of Single Receptor when Excited at Diode Port Near Resonance	22
4-2	$ S_{12} $ Between Two Receptors Spaced by λ_0 in the E- and H-Plane Configurations	23
4-3	Maximum Stable Power Gain for Two PBTs Fabricated Using Si-Doped, OMCVD Overgrowth	25
4-4	Energy Separation Between Light- and Heavy-Hole Exciton Emission in $\text{Ga}_{1-x}\text{Al}_x\text{As}$ Quantum Wells	27
5-1	Cross Section of a Superconductive Stripline Delay Line on Bonded and Etched Silicon Epilayers. The Inset Shows the Passivated Ground Plane.	30
5-2	Auger Profile of Superconducting Ground Planes After Bonding to Pyrex: (a) Nb Ground Plane; (b) NbN (400 Å)/Nb (3000 Å)/NbN (400 Å)/Nb (150 Å) Ground Plane. The High Background Level of Silicon Is an Artifact of the High Ion-Beam Current Used to Profile This Sample.	31
5-3	A Simple BAW Device, a Bandpass Filter. The Stored Grating Is Created by the Laser Illumination. The Grating Interacts Strongly with the Incident Acoustic Beam and Reflects the Energy Contained in a Narrow Frequency Band, thus Forming a Bandpass Filter.	33
5-4	(a) Photograph of Multiple Reflections of an Acoustic Wave from Back Face of Sample. A Single Transducer Was Used for Both Input and Output. (b) Same as (a) but with 10 Times Larger Gain. The Reflections from the Back Face Are Off Scale and Not Visible. The Spaces Between Back-Face Reflections Are Filled with the Reflection from the Hologram.	34

Figure No.		Page
5-5	Schematic of a Setup to Obtain the Convolution of an Image with an Arbitrary Positive Function. The Scale of the Kernel Function Is Changed by Moving the Camera Along the Optical Axis.	36
5-6	Modified Arrangement for Optical Convolution. The Center of the Screen Is Placed on the Optical Axis at a Distance f from the Lens. With This Arrangement, the Scale of the Kernel Function Can Be Varied Without Changing the Magnification of the Image.	37
5-7	(a) Original Focused Image Used for the DOG. (b) Results of the Edge Extraction Using Optical Gaussian Convolutions. (c) Results of Edge Extraction Using Computer-Calculated Gaussian Convolutions of the Original Picture.	38
5-8	Narrowband Exciser	40
5-9	Phase-Locked Loop	41
5-10	Phase-Locked-Loop Output Spectrum. Note that a 10-kHz Measurement Bandwidth Is Used.	42
5-11	Phase Error Response to an (a) 100-MHz Frequency Step, and (b) 10-MHz Frequency Step	43

LIST OF TABLES

Table No.		Page
2-1	Type II Frequency Conversion in KTP	11
4-1	Comparison of Microwave Characteristics of Si-Doped, OMCVD-Overgrown, GaAs PBTs	25

INTRODUCTION

1. SOLID STATE DEVICE RESEARCH

Low-dark-current (2.5×10^{-5} A/cm²), high-speed (50-ps) n⁺InP/InGaAs/p⁺InP double-heterojunction PIN photodetectors have been grown by special liquid-phase-epitaxial techniques. This development allows front-illumination, which substantially simplifies device fabrication and operation. Good control of pn junction location and layer thickness permits optimization for high-speed performance.

2. QUANTUM ELECTRONICS

The optical properties of Er:YAG laser crystals have been measured, and laser gain and absorption parameters have been calculated. We found that, with diode laser pumping at 1.452 μm , moderate gain at 1.645 μm should be possible at room temperature and high gain should be obtainable at 195 K.

A study has been initiated for potential nonlinear materials that can be used to achieve efficient frequency tripling of 1.645- μm radiation at high average-power levels. Initial studies indicate that KTiPO₄ is a promising material for this purpose, and an effort is under way to measure relevant parameters.

3. MATERIALS RESEARCH

Test chips containing a 120-gate-array circuit and a two-phase dynamic shift register have been fabricated in Si-on-insulator films prepared by zone-melting recrystallization using graphite strip heaters. Both circuits give good high-speed performance, showing that their operation is not significantly affected by the subboundaries present in the films, although the circuit yield is still limited by surface defects such as voids and protrusions.

The results of optical absorption and electrical measurements made on crystals of V-doped InP grown by the liquid-encapsulated Czochralski method show that the electronic level of V in InP lies lower than about 0.25 eV above the valence band edge. Therefore, semi-insulating InP cannot be obtained by V doping.

4. MICROELECTRONICS

Impedance and mutual-coupling measurements have been made on planar receptor circuits at a scale-model frequency of 3.2 GHz. The results suggest how improvements may be made in the sensitivity and resolution of planar heterodyne imaging arrays operating at millimeter wavelengths.

Reproducible fabrication of high-frequency permeable-base silicon transistors (PBTs) with maximum stable power gains as high as 20.7 and 14.1 dB at 18 and 26.5 GHz, respectively, have been observed. The large, reproducible power gains of these devices exceed the microwave performance of all PBTs fabricated to date.

Photoluminescence data of quantum wells in GaAs-Ga_{1-x}Al_xAs have been combined with an accurate theory of two-dimensional excitons to provide a convenient technique for determining the dimension of a quantum well in these materials for wells ~40 to 200 Å wide.

5. ANALOG DEVICE TECHNOLOGY

Thin (15-μm) silicon substrates bonded to glass support wafers are being developed for miniature superconductive microwave delay lines. Niobium ground planes at the silicon/glass interface have been discovered to become oxidized during the bonding procedure. Niobium nitride has proven to be an effective diffusion barrier, preventing this oxidation and preserving the low conduction loss of the niobium.

Reflections of bulk acoustic waves from optically generated holograms in Fe-doped LiNbO₃ have been observed and measured. Holographic gratings with a period of 3.6 μm were written by exposure to an Ar laser and were found to have a reflection coefficient per grating element of 1.5×10^{-4} . Such reflections can be utilized to produce a number of different signal-processing devices such as band-pass filters, resonators, and delay lines, with several-gigahertz bandwidth and several microseconds of delay.

A simple apparatus based on classical optics has been developed that performs the convolution of an image with an arbitrary positive, space-limited function. The convolution of an image with Gaussian functions of widely varying widths has been demonstrated by using a single screen with a transmissivity that follows a truncated Gaussian function. By taking the difference of appropriate pairs of convolved images according to the difference-of-Gaussians (DOG) algorithm, edge detection has been performed.

A phase-locked loop has been developed for signal excision in wideband receiver applications. The system has three internal loops and will set on frequency in less than 20 μs in a band from 250 to 350 MHz with a phase error less than 3° and a spurious level, measured over any 10-kHz-wide band, of less than -55 dB with respect to the carrier.

REPORTS ON SOLID STATE RESEARCH

1 May through 31 July 1985

PUBLISHED REPORTS

Journal Articles

JA No.

5518	Zone-Melting Recrystallization of Si Films on SiO ₂	B-Y. Tsaur	Chapter in <i>Silicon-on-Insulator: Its Technology and Applications</i> , S. Furukawa, Ed. (KTK Scientific Publishers, Tokyo, 1985), p. 101
5651	Detrimental Optical Properties of Germanium Intermediate Layers in Monolithic Tandem Solar Cell Structures	G.W. Turner	Solar Cells 14 , 139 (1985), DTIC AD-A158747
5674	Superconductive Chirp-Transform Spectrum Analyzer	R.S. Withers S.A. Reible	IEEE Electron. Device Lett. EDL-6 , 261 (1985)
5695	Summary Abstract: Laser-Microchemical Reactions for Maskless Device Processing: Surface Modifications for Selected-Area Growth	D.J. Ehrlich J.Y. Tsao	J. Vac. Sci. Technol. A 3 , 904 (1985), DTIC AD-A156612
5720	Enhanced Quantum Efficiency Internal Photoemission Detectors by Grating Coupling to Surface Plasma Waves	S.R.J. Brueck V. Diadiuk T. Jones W. Lenth	Appl. Phys. Lett. 46 , 915 (1985)
5731	Persistent Photoconductivity in Quantum Well Resonators	T.C.L.G. Sollner H.Q. Le C.A. Correa W.D. Goodhue	Appl. Phys. Lett. 47 , 36 (1985), DTIC AD-A156611
5732	Holographic-Grating Acoustic Devices	D.E. Oates P.G. Gottschalk P.V. Wright	Appl. Phys. Lett. 46 , 1125 (1985), DTIC AD-A156613

JA No.

5741 Laser Linewidth

A. Mooradian

Phys. Today **38**, 42 (1985),
DTIC AD-A157970**Meeting Speeches****MS No.**6500 Effect of Low Temperature
Preanneal and High Temperature
Rapid Thermal Annealing on
Arsenic-Implanted SiliconR. Kwor*
D.L. Kwong*
C.C. Ho*
B-Y. Tsaur
S. Baumann*J. Electrochem. Soc. **132**,
1201 (1985)6598 Growth of Semiconductor/
Insulator Structures — GaAs/
Fluoride/GaAs (001)P.W. Sullivan*
J.E. Bower*
G.M. MetzeJ. Vac. Sci. Technol. B
3, 500 (1985)6719 Applications of Beam-Solid
Interactions in Semiconductor
Material and Device
Processing

J.C.C. Fan

Mat. Res. Soc. Symp. Proc.,
Vol. 35, Boston, 26-30 No-
vember 1984, pp. 39-50,
DTIC AD-A1565396720 SOI Technologies: Device
Applications and Future
Prospects

B-Y. Tsaur

Mat. Res. Soc. Symp. Proc.,
Vol. 35, Boston, 26-30 No-
vember 1984, pp. 641-652,
DTIC AD-A1563096722 Recent Advances in Si and Ge
Zone-Melting RecrystallizationC.K. Chen
M.W. Geis
H.K. Choi
B-Y. Tsaur
J.C.C. FanMat. Res. Soc. Symp. Proc.,
Vol. 35, Boston, 26-30 No-
vember 1984, pp. 613-618,
DTIC AD-A157084

* * * * *

UNPUBLISHED REPORTS**Journal Articles****JA No.**5730 Applications of SAW Convolvers
to Spread-Spectrum Communi-
cation and Wideband RadarI. Yao
J.H. CafarellaAccepted by IEEE Trans.
Sonics Ultrason.

* Author not at Lincoln Laboratory.

JA No.

5736	Laser Remote Sensing of Atmospheric Ammonia Using a CO ₂ LIDAR System	A.P. Force* D.K. Killinger W.E. DeFeo N. Menyuk	Accepted by Appl. Opt.
5737	Measurement of Surface Diffusion by Laser-Beam-Localized Surface Photochemistry	J.Y. Tsao H.J. Zeiger D.J. Ehrlich	Accepted by Surf. Sci.
5739	An Investigation of the Co:MgF ₂ Laser System	P.F. Moulton	Accepted by IEEE J. Quantum Electron.
5742	The SAW/FET Signal Processor	J.B. Green G.S. Kino*	Accepted by IEEE Trans. Sonics Ultrason.
5744	18.5 dB Gain at 18 GHz with a GaAs Permeable Base Transistor	C.O. Bozler M.A. Hollis K.B. Nichols S. Rabe A. Vera C.L. Chen	Accepted by IEEE Electron. Device Lett.
5760	Metal-Oxide-Semiconductor Field-Effect Transistors Fabricated Using Self-Aligned Silicide Technology	B-Y. Tsaur C.H. Anderson, Jr.	Accepted by Appl. Phys. Lett.
5761	Theory of the Effect of Traps on the Spectral Characteristics of Diode Lasers	H.J. Zeiger	Accepted by Appl. Phys. Lett.
5764	Submillimeter-Wave Heterodyne Spectroscopy With a Compact Solid State Radiometer	J.A. Taylor P.E. Tannenwald N.R. Erickson* G.F. Dionne J.F. Fitzgerald	Accepted by Int. J. Infrared and Millimeter Waves
5771	Superconductive Analog Signal Processing Devices	R.S. Withers	Accepted by Superconductive Technology in Review

* Author not at Lincoln Laboratory.

Meeting Speeches*

MS No.

6674D	Monolithic Integration of GaAs and Si	J.C.C. Fan	}	American Vacuum Society Symposium on Frontiers of Silicon, Murray Hill, New Jersey, 19 June 1985
6720B	SOI Technologies: Device Applications and Future Prospects	B-Y. Tsaur		
6702A	Wideband SAW/FET Programmable Transversal Filter	D.E. Oates D.L. Smythe J.B. Green		Boston IEEE Sonics and Ultrason. Group, Lincoln Laboratory, May 1985
6718B	Recent Advances in SOI Films Produced by Zone-Melting Recrystallization	M.W. Geis C.K. Chen H.I. Smith R.W. Mountain C.L. Doherty		Seminar, Dow-Corning, Saginaw, Michigan, 28 May 1985
6720A	SOI Technologies: Device Applications and Future Prospects	B-Y. Tsaur		New England Combined Chapter of the American Vacuum Society, Nashua, New Hampshire, 10-11 June 1985
6750A	Laser Direct Patterning: New Processing Technology and Device Applications	D.J. Ehrlich		MRS Annual Symposium, Strasbourg, France, 13-15 May 1985
6827	Wide-Band Integrated-Optics Electrooptic Intensity Modulator for $\lambda = 3.39 \mu\text{m}$ Operation	R.H. Rediker R.A. Becker T.A. Lind	}	CLEO '85, Baltimore, Maryland, 21-24 May 1985
6834	Transient Carrier Density and Light Output Measurements of Pulsed Diode Lasers	B.C. Johnson A. Mooradian		

* Titles of Meeting Speeches are listed for information only. No copies are available for distribution.

MS No.

6835	Dual Function Mixer Circuit for Millimeter Wave Transceiver Applications	A. Chu W.E. Courtney L.J. Mahoney M.J. Manfra A.R. Calawa	1985 IEEE Microwave and Millimeter Wave Monolithic Circuit Symposium, St. Louis, Missouri, 3-4 June 1985
6841	Hybrid Analog/Digital Signal Processing for Data Communications in a Multipath Channel	J.H. Fisher J.H. Cafarella	North American Radio Science Meeting, Vancouver (B.C.), Canada, 17-21 June 1985
6849	The Contrast of Ion Beam Stencil Masks	J.N. Randall L.A. Stern J.P. Donnelly	EIPB '85, Portland, Oregon, 28-31 May 1985
6860	Anisotropic Etching of Al by Directed Cl ₂ Flux	N.N. Efremow M.W. Geis R.W. Mountain G.A. Lincoln J.N. Randall N.P. Economou	
6862	Sub-100-nm-Wide, Deep Trenches Defined by Reactive-Ion-Etching	S.W. Pang J.N. Randall M.W. Geis	
6864	Focused Ion Beams Applied to Integrated Circuit Restructuring	J. Melngailis C.R. Musil* E.H. Stevens* M. Utlaut* E.M. Kellogg* R. Post* M.W. Geis R.W. Mountain	
6868	Hot Jet Etching of GaAs and Si	M.W. Geis N.N. Efremow G.A. Lincoln	

* Author not at Lincoln Laboratory.

MS No.

6875	Optimization of Solvent Development in PMMA — E-Beam and Ion Beam — Graft Lithography	S.Y. Kim* J. Choi* D. Pulver* J.A. Moore* J.C. Corelli* A.J. Steckl* J.N. Randall	EIPB '85, Portland, Oregon, 28-31 May 1985
6880	Excimer-Laser Etching of Diamond by Direct Writing and Optical Projection	M. Rothschild C. Arnone D.J. Ehrlich	
6849A	The Contrast of Ion Beam Stencil Masks	J.N. Randall L.A. Stern J.P. Donnelly	Seminar, Hughes Research, Malibu, California, 3 June 1985
6850	Dry Etching Techniques for GaAs: The Critical Issue of Surface Damage	S.W. Pang	Electrochemical Society Meeting, Toronto, Canada, 12-17 May 1985
6884	Selective Tungsten Deposition on Laser-Direct-Written Polysilicon Interconnections	J.G. Black D.J. Ehrlich J.H.C. Sedlacek A. Feinerman* H.H. Busta*	Electronic Materials Conference, Boulder, Colorado, 21 June 1985
6905	Chaotic Pulsation of Semiconductor Lasers with a Proton-Bombarded Segment	M. Kuznetsov* D.Z. Tsang J.N. Walpole Z.L. Liao E.P. Ippen*	Instabilities and Dynamics of Lasers and Nonlinear Optical Systems, Rochester, New York, 18-21 June 1985
6906	High Performance Si Permeable Base Transistors	D.D. Rathman R.W. Mountain	Device Research Conference, Boulder, Colorado, 17-19 June 1985
6916	Laser Probes of Semiconductor Materials and Devices	S.R.J. Brueck	Seminar, IBM Europe Institute, Lech, Austria, 5-9 August 1985
6920A	Fundamental Spectral Width of Laser Light	A. Mooradian	SEICOLS '85, Maui, Hawaii, 23-28 June 1985

* Author not at Lincoln Laboratory.

MS No.

6933	Persistent Photoconductivity in Resonant Tunneling Structures: Toward a Resonant Tunneling Transistor	T.C.L.G. Sollner H.Q. Le C.A. Correa W.D. Goodhue	IEEE Cornell Conference on Advanced Concepts in High Speed Semiconductors and Circuits, Ithaca, New York, 29-31 July 1985
6938	Effect of Reactive Gases on GaAs Surface Damage Induced by Reactive-Ion Etching and Ar Sputter Etching	S.W. Pang	
6940	Fabrication and Performance of GaAs Permeable Base Transistors	K.B. Nichols M.A. Hollis C.O. Bozler R.P. Gale	
6934	Superconductive Analog Signal Processing Devices	A.C. Anderson L.N. Smith S.A. Reible J.B. Green R.S. Withers R.W. Ralston	U.S.-Japan Workshop on Josephson-Junction Technology, Honolulu, Hawaii, 17-19 June 1985
6939	Surface-Emitting GaInAsP Lasers	Z.L. Liao J.N. Walpole	IEEE Lasers and Electro-Optics Society 1985 Workshop on Semiconductor Lasers, Baltimore, Maryland, 19 May 1985
6964	An Adaptive Clutter Canceler for Radars Using Nonrepeating Pseudonoise Waveforms	C.A. Bouman	Tri-Service Radar Symposium, Peterson Air Force Base, Colorado, 18-20 June 1985

ORGANIZATION

SOLID STATE DIVISION

A.L. McWhorter, *Head*
I. Melngailis, *Associate Head*
E. Stern, *Associate Head*
J.F. Goodwin, *Assistant*

P.E. Tannenwald, *Senior Staff*

QUANTUM ELECTRONICS

A. Mooradian, *Leader*
P.L. Kelley, *Associate Leader*

Barch, W.E.	Johnson, B.C. [†]
Belanger, L.J.	Killinger, D.K.
Brueck, S.R.J.	Le, H.
Bushee, J.F., Jr.	Menyuk, N.
DeFeo, W.E.	Rosenbluh, M.*
Feldman, B.	Sanchez-Rubio, A.
Hancock, R.C.	Sharpe, K.A.
Harrison, J.*	Sullivan, D.J.

ELECTRONIC MATERIALS

A.J. Strauss, *Leader*
J.C.C. Fan, *Associate Leader*
B-Y. Tsaur, *Assistant Leader*
H.J. Zeiger, *Senior Staff*

Anderson, C.H., Jr.	Kolesar, D.F.
Button, M.J.	Krohn, L., Jr.
Chen, C.K.	Mastromattei, E.L.
Choi, H.K.	McClelland, R.W.
Connors, M.K.	Nitishin, P.M.
Delaney, E.J.	Pantano, J.V.
Fahey, R.E.	Tracy, D.M.
Finn, M.C.	Turner, G.W.
Gale, R.P.	Wang, C.A.
Iseler, G.W.	Windhorn, T.H.
King, B.D.	

APPLIED PHYSICS

R.C. Williamson, *Leader*
D.L. Spears, *Assistant Leader*
T.C. Harman, *Senior Staff*
R.H. Rediker, *Senior Staff*

Anderson, K.K. [†]	Hovey, D.L.	Reeder, R.E.
Chan, Sokuen	Johnson, L.M.	Schloss, R.P. [†]
Cox, C.H., III	Liau, Z.L.	Tsang, D.Z.
DeMeo, N.L., Jr.	Lind, T.A.	Walpole, J.N.
Diadiuk, V.	McBride, W.F.	Whitaker, N. [†]
Donnelly, J.P.	Metze, G.M.	Woodhouse, J.D.
Duffy, P.E.	Molter, L.A. [†]	Yap, D. [†]
Ferrante, G.A.	O'Donnell, F.J.	Yee, A.C.
Groves, S.H.	Plonko, M.C.	

* Summer Staff

† Research Assistant

ANALOG DEVICE TECHNOLOGY

R.W. Ralston, *Leader*

R.S. Withers, *Assistant Leader*

Anderson, A.C.
Arsenault, D.R.
Boisvert, R.R.
Bouman, C.A.
Brogan, W.T.
Delaney, M.A.*
Denneno, A.P.
DiIorio, M.S.
Dolat, V.S.

Fischer, J.H.
Fitch, G.L.
Flynn, G.T.
Green, J.B.
Hauser, E.M.
Holtham, J.H.
Kernan, W.C.
Lattes, A.L.
Macedo, E.M., Jr.

Macropoulos, W.
Maiocco, L.B.
Marden, J.A.
Munroe, S.C.
Oates, D.E.
Sage, J.P.
Thompson, K.E.†
Yao, I.

MICROELECTRONICS

W.T. Lindley, *Leader*

D.J. Ehrlich, *Assistant Leader*

B.B. Kosicki, *Assistant Leader*

R.A. Murphy, *Assistant Leader*

Arnone, C.
Astolfi, D.K.
Bales, J.W.*
Bennett, P.C.
Black, J.G.
Bozler, C.O.
Burke, B.E.
Calawa, A.R.
Chen, C.L.
Chiang, A.M.
Clifton, B.J.
Correa, C.A.
Daniels, P.J.
Doran, S.P.
Durant, G.L.
Efremow, N.N., Jr.
Felton, B.J.
Gajar, S.*

Geis, M.W.
Goodhue, W.D.
Gray, R.V.
Hollis, M.A.
Lax, B.†
LeCoz, Y.L.*
Lincoln, G.A., Jr.
Lyszczarz, T.M.
Mahoney, L.J.
Manfra, M.J.
Melngailis, J.†
McGonagle, W.H.
Mims, V.†
Mountain, R.W.
Nichols, K.B.
Oliver, S.
Paczuski, M.

Pang, S.W.
Parker, C.D.
Piacentini, W.J.
Pichler, H.H.
Rabe, S.
Randall, J.N.
Rathman, D.D.
Reinold, J.H.
Rothschild, M.
Sedlacek, J.H.C.
Smythe, D.L., Jr.
Sollner, T.C.L.G.
Stern, L.A.
Sullivan, D.J.
Taylor, J.A.*
Vera, A.
Wilde, R.E.

* Research Assistant

† Staff Associate

‡ Part Time

1. SOLID STATE DEVICE RESEARCH

1.1 DOUBLE-HETEROSTRUCTURE InGaAs/InP PIN PHOTODETECTORS

$\text{In}_{0.53}\text{Ga}_{0.47}\text{As}/\text{InP}$ avalanche and PIN photodetectors are attractive for applications involving wavelengths shorter than $1.7 \mu\text{m}$. Most InGaAs detectors reported to date¹⁻⁴ have been single-heterojunction devices with the disadvantage of requiring back-side illumination. Also, most have had the pn junction deliberately displaced from the heterointerface. Here, we report results on high-performance PIN photodetectors made from $n^+\text{InP}/\text{InGaAs}/p^+\text{InP}$ (substrate) double heterostructures in which the pn junction is grown and coincides with the heterojunction. This structure does not require a diffusion step in fabrication and allows for greater control of junction location and layer thickness, which, in turn, makes it possible to minimize device response time. For the ultimate in high-speed performance, back-side illumination must be used because the small active areas required are entirely covered by the top contact. However, front-illuminated detectors, which are considerably easier to fabricate and use, are shown to exhibit response times of ≈ 50 ps and are predicted to be capable of response times of 30 ps.

Figure 1-1 shows the basic inverted mesa device structure. The InGaAs and $n^+\text{InP}$ layers were grown by liquid phase epitaxy (LPE) directly on the liquid-encapsulated-Czochralski (LEC)-grown p^+ substrate. Two forms of InGaAs were used: (a) an n^- layer, unintentionally doped, with

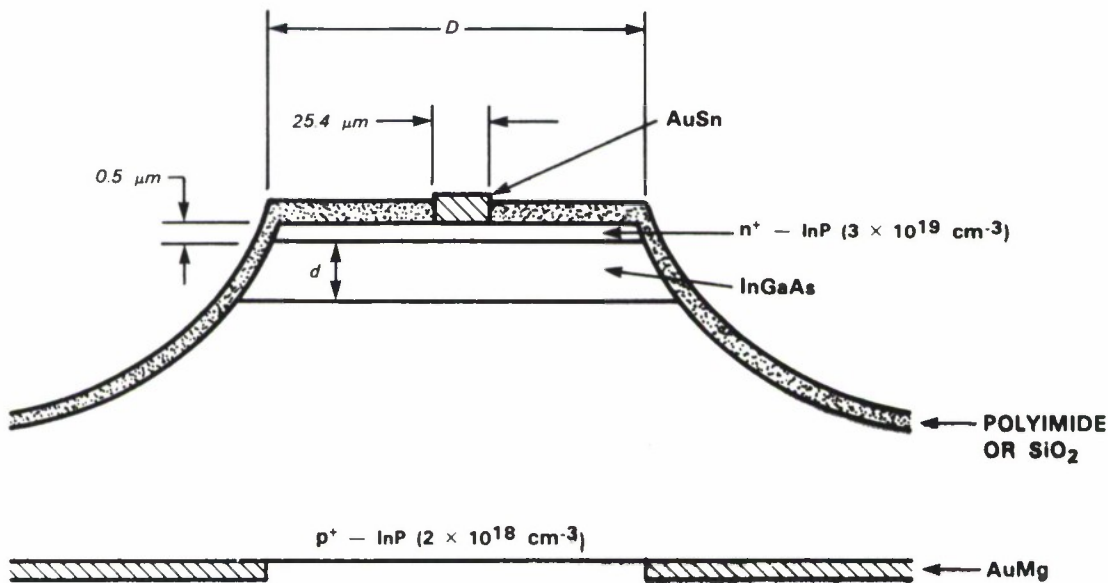
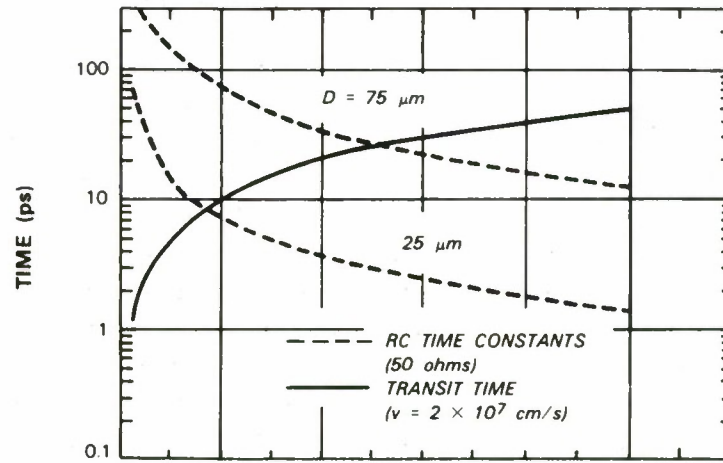
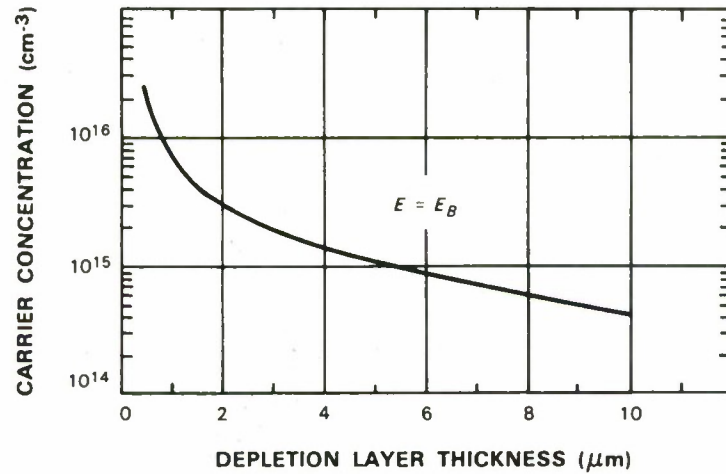


Figure 1-1. Inverted-mesa double-heterostructure PIN photodetector. The InGaAs layer thickness d was 1.5 to $5 \mu\text{m}$ and its carrier concentration was either (a) $6 \times 10^{14} \text{ cm}^{-3} < n^- < 1 \times 10^{16} \text{ cm}^{-3}$, or (b) $n = p = 1 \times 10^{12} \text{ cm}^{-3}$. Device diameters D ranged from 6 to $75 \mu\text{m}$.



(a)



(b)

Figure 1-2. Calculated curves showing factors which are important in design of high-speed PIN photodetectors. (a) RC time constant, for two device diameters D , and transit time vs depletion depth. (b) Depletion depth at breakdown for various carrier concentrations.

concentrations between 6×10^{14} and $1 \times 10^{16} \text{ cm}^{-3}$, depending on the conditions of the pre-growth bake⁵; and (b) a semi-insulating (SI) layer with $n = p = 10^{12} \text{ cm}^{-3}$ and $\rho = 2500 \text{ } \Omega\text{-cm}$ produced by Fe doping.⁶ Normally, the InGaAs layer is dissolved when an attempt is made to overgrow an InP layer by LPE, which is the reason the single heterostructure has been used in reported work.¹⁻⁴ Here, we have avoided this problem by growing the InP cap layer from a Sn-rich, rather than In-rich, solution.⁷

For a high-speed PIN device, several considerations are important in selecting the carrier concentration and thickness of the InGaAs layer; they are summarized in Figure 1-2. Figure 1-2(a) shows the calculated RC time constant for two device diameters and the calculated transit time as functions of the active layer thickness, assuming it to be fully depleted. R is set by the 50- Ω external load resistor, and C is the junction capacitance. The transit time is calculated by dividing the depletion width by the saturation velocity [$2 \times 10^7 \text{ cm/s}$ (Reference 8)]. Figure 1-2(b) relates the carrier concentration to the depletion width at breakdown.⁹ These curves can be used to design a PIN detector. For example, if a certain device diameter is required, the response time can be minimized by selecting a thickness from Figure 1-2(a) for which the RC and transit times are comparable. It is necessary for the active layer to be fully depleted to prevent the presence of slow diffusion current components, and an upper limit on the net carrier concentration for this can be determined from Figure 1-2(b). For the devices reported here, the InGaAs thickness ranged from 1.5 to 5 μm , depending on the intended device diameter.

The devices had circular areas ranging in diameter from 6 to 150 μm and were fabricated with standard photolithographic techniques. Plated AuSn dots (6 to 25 μm in diameter) and evaporated AuMg (patterned to allow back-illumination) were alloyed to form ohmic contacts. The capability of back-illumination affords the additional testing flexibility of being able to inject carriers immediately adjacent to the pn junction. However, front-illumination is much more convenient from the standpoint of mounting, packaging, and aligning and, even on 75- μm -dia. devices (which can easily be front-illuminated), response times as short as 30 ps are predicted [see Figure 1-2(b)]. Individual devices were cleaved and mounted in high-frequency microstrip packages (shown in Figure 1-3) which allowed both front- and back-illumination.

Figure 1-4 shows the carrier concentration as a function of distance from the pn junction for a $n^+n^-p^+$ device. The carrier concentration in the n^- region is uniform and the grown n^-n^+ interface is sharp. The InGaAs layer thickness derived from these measurements agrees well with the values obtained directly by cleaving and staining the layer cross section.

Figure 1-5 shows the capacitance vs voltage characteristic for a device with Fe-doped ternary layer. As expected for the very low background carrier concentration of the SI material, the capacitance is a function of voltage only at low bias ($<0.5 \text{ V}$). This indicates that the depletion region is not widening with voltage, i.e., that punch-through has been achieved and the active layer is fully depleted.

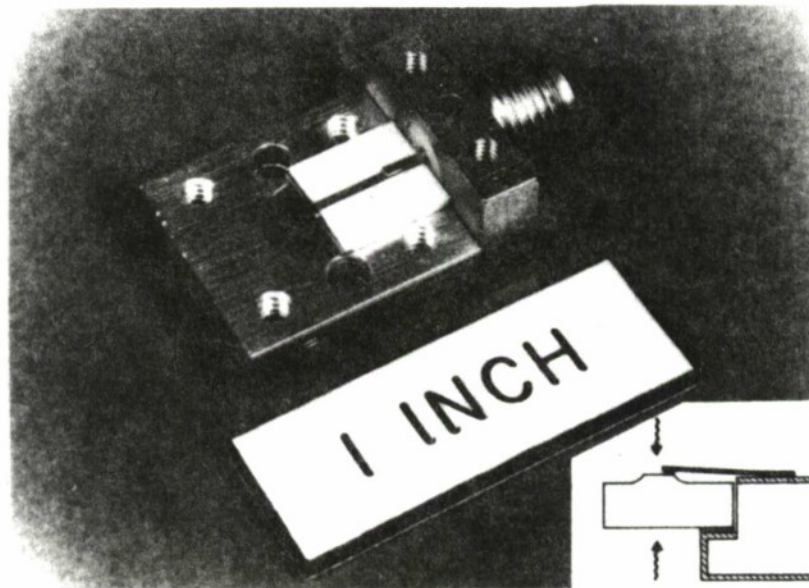


Figure 1-3. Photograph of detector package. The device chip is mounted (inset) on the 50- Ω alumina microstrip carrier (white square at center) such that both front- and back-illumination are possible.

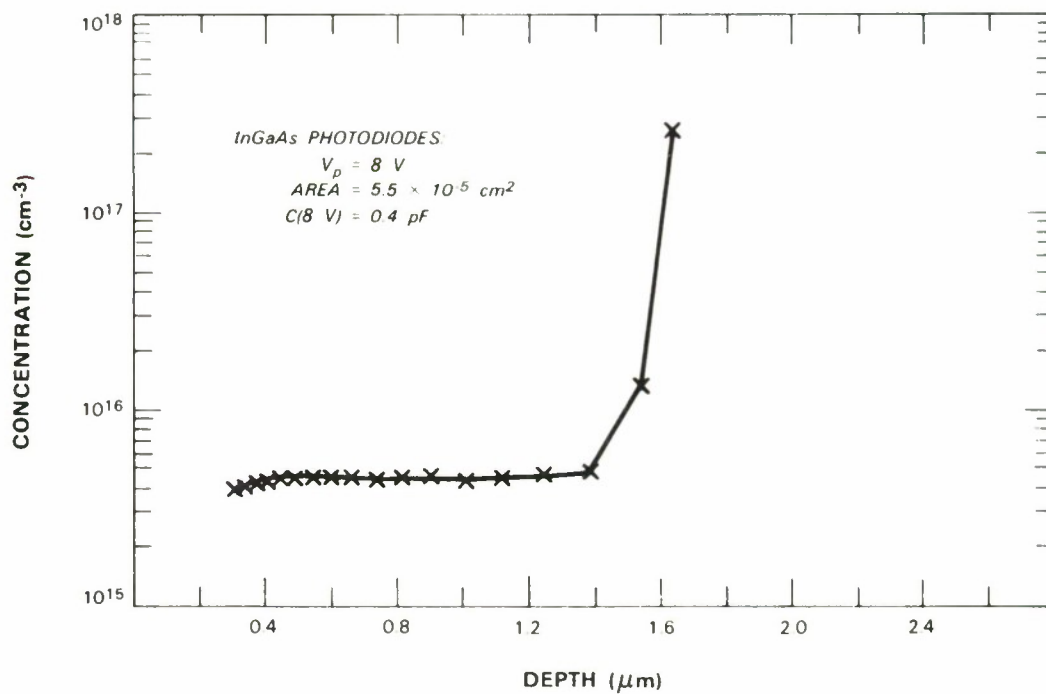
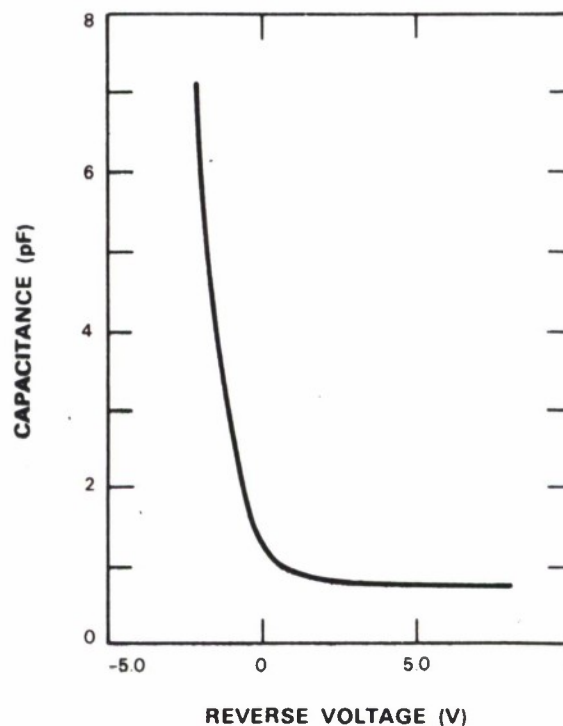


Figure 1-4. InGaAs carrier concentration vs distance from pn junction for n-InGaAs double-heterostructure device. The width of the n^+n interface and the final value of the carrier concentration are limited by the CV probing method used.

Figure 1-5. Capacitance vs voltage for SI-InGaAs double-heterostructure device near $V = 0$. The lack of variation with reverse voltage indicates that the InGaAs layer is fully depleted at $V = -0.5$ V.



Typical I-V characteristics, in the dark and under illumination, of a n^+n-p^+ detector are shown in Figure 1-6. Similar behavior was observed for the Fe-doped devices. The dark-current density at punch-through ($V_p = 8$ V) is 2.6×10^{-5} A/cm², which is comparable to that obtained on single-heterojunction devices.¹⁰ Two distinct regions are apparent in this curve. At low bias (<15 V), the dark current varies slowly with voltage and is due to generation within the depletion region. For higher biases, the tunneling current becomes dominant and increases nearly exponentially with voltage.¹¹ The photocurrent was measured by illuminating the detector with $\lambda = 1.15$ - μ m light from a He-Ne laser. The curve shown corresponds to front-illumination, but similar behavior was observed when the light was incident from the back. The photocurrent is nearly independent of bias, as would be expected with the hole diffusion length greater than the active layer width.¹² The external quantum efficiency, measured using a calibrated Ge photodiode, was 59 percent from the front and 55 percent from the back, on devices without antireflection coating. This indicates that the thin, but heavily doped, n^+ InP layer is at least as transparent as the more lightly doped (but thicker) p^+ substrate.

Two types of high-frequency measurements were carried out on these devices. To test pulse response, a comb-generator-driven InGaAsP laser ($\lambda = 1.24$ μ m) was used as a source, and the output of the detector was fed to a sampling oscilloscope. The results obtained with a 75- μ m-dia. n^+ Si p^+ detector illuminated from the front are shown in Figure 1-7. The full-width-at-half-maximum (FWHM) is 52 ps. A similar result is obtained when the electrical output of the comb generator is directly connected to the sampling oscilloscope, and we conclude that the response is not being limited by the detector. Measurements in the frequency domain were carried out using

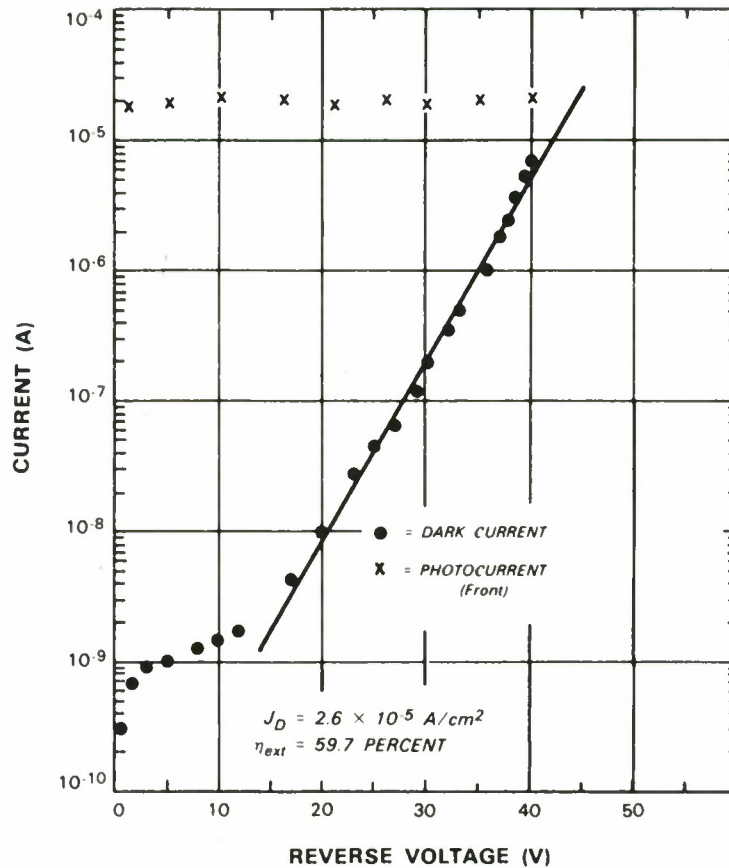


Figure 1-6. Current vs reverse-voltage characteristics for $n\text{-InGaAs}$ device in the dark and under front-illumination. The dark current shows the generation and tunneling (exponential) regimes. The voltage independence of the photocurrent is a result of long diffusion lengths relative to the layer thickness.

an intracavity-loss modulator laser¹³ as a source. Figure 1-8 shows the response of a 25- μm -dia. back-illuminated $n^+n\text{-p}^+$ detector at 10 GHz. The full depth of modulation observed indicates that all components in the source-detector system respond at this frequency (which is equivalent to $\approx 50\text{-ps}$ pulse response). These measurements have recently been extended to frequencies up to 13 GHz (Reference 14), but network analyzer measurements indicate package roll-off above this frequency. An accurate assessment of the detector high-speed capabilities using these techniques is difficult because it is the total system response that is measured. Correlation techniques,¹⁵ which are presently being implemented, will be useful in getting around these limitations and should lead to a more definitive statement of the high-frequency performance of these devices.

V. Diadiuk
S.H. Groves

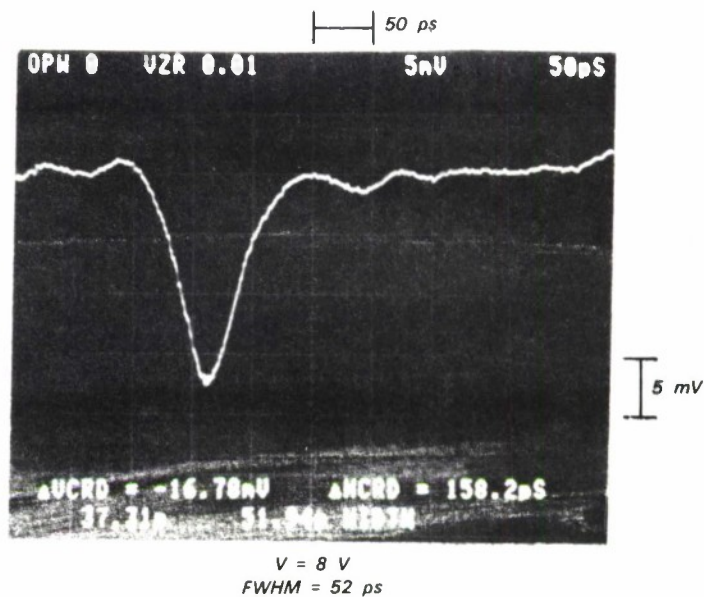


Figure 1-7. Response of front-illuminated SI-InGaAs detector to comb-generator-driven InGaAsP laser. System-limited FWHM is 52 ps.

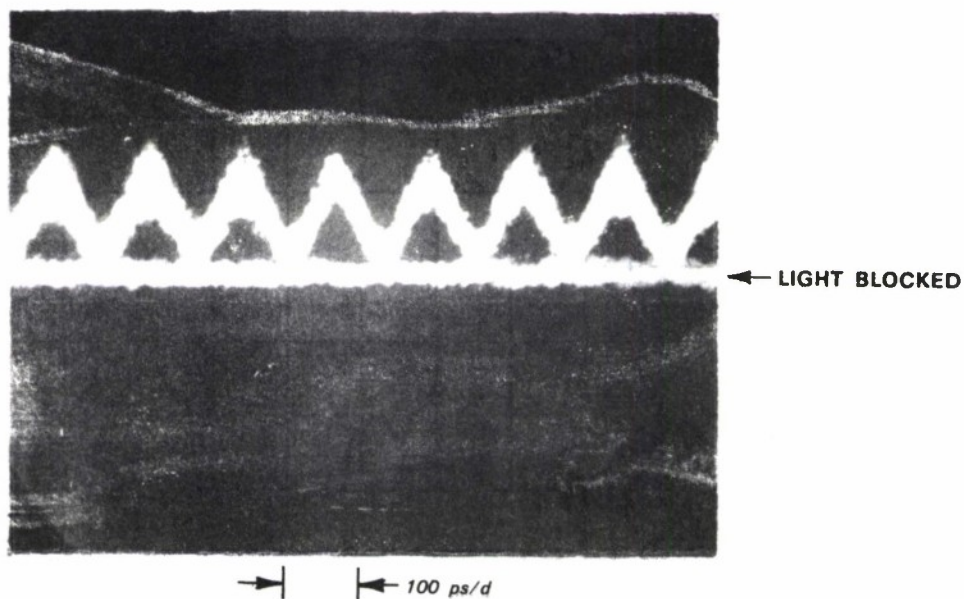


Figure 1-8. Response of back-illuminated n-InGaAs device to 10-GHz output of intracavity-loss modulator laser.

REFERENCES

1. H. Ando, Y. Yamauchi, H. Nakagome, N. Susa, and H. Kanbe, IEEE J. Quantum Electron. **QE-17**, 250 (1981).
2. S.R. Forrest, R.G. Smith, and O.K. Kim, IEEE J. Quantum Electron. **QE-18**, 2040 (1982).
3. T.P. Li, C.A. Burrus, K. Ogawa, and A.G. Dentai, Electron. Lett. **17**, 431 (1981).
4. J.E. Bowers, C.A. Burrus, and R.S. Tucker, OSA Topical Meeting Tech. Digest "Picosecond Electronics and Optoelectronics," Paper ThA3, Incline Village, Nevada, 13-15 March 1985.
5. S.H. Groves and M.C. Plonko, J. Cryst. Growth **54**, 81 (1981), DTIC AD-A107233.
6. S.H. Groves, V. Diadiuk, M.C. Plonko, and D.L. Hovey, Appl. Phys. Lett. **46**, 78 (1985), DTIC AD-A150697.
7. S.H. Groves and M.C. Plonko, Appl. Phys. Lett. **38**, 1003 (1981), DTIC AD-A105410.
8. T.H. Windhorn, L.W. Cook, and G.E. Stillman, J. Electron. Mater. **11**, 1065 (1982).
9. S.M. Sze, *Physics of Semiconductor Devices* (Wiley, New York, 1981), p. 104.
10. R.F. Leheny, R.E. Nahory, and M.A. Pollack, Electron. Lett. **15**, 713 (1979).
11. S.R. Forrest, IEEE J. Quantum Electron. **QE-17**, 217 (1981).
12. V. Diadiuk, S.H. Groves, C.A. Armiento, and C.E. Hurwitz, Appl. Phys. Lett. **42**, 892 (1983), DTIC AD-A147806.
13. D.Z. Tsang, J.N. Walpole, S.H. Groves, J.J. Hsieh, and J.P. Donnelly, Appl. Phys. Lett. **38**, 120 (1981), DTIC AD-A103344.
14. D.Z. Tsang (to be published).
15. D.H. Auston and P.R. Smith, Appl. Phys. Lett. **41**, 599 (1982).

2. QUANTUM ELECTRONICS

2.1 Er:YAG LASER CRYSTAL CHARACTERIZATION

Er:YAG is under study as a potential optical pump source. The optical absorption properties of Er:YAG samples obtained from several boules have been measured at room temperature, 195 K, and 77 K.

Figure 2-1 shows the measured absorption curve of a 5-mm-thick sample of 1% Er-doped Er:YAG (1.4×10^{20} Er^{+3} ions/ cm^3) and the associated energy level diagram. The absorption cross section at $1.45 \mu\text{m}$ was measured for a single line to be $6.3 \times 10^{-20} \text{ cm}^2$ at 300 K and $8.4 \times 10^{-20} \text{ cm}^2$ at 195 K; at $1.645 \mu\text{m}$, it was $1.9 \times 10^{-20} \text{ cm}^2$ at 300 K and $2.9 \times 10^{-20} \text{ cm}^2$ at 195 K. These absorption values were used along with the appropriate population distribution within the ground state manifold to calculate expected gains for an Er:YAG transition. For an assumed pump intensity of 100 W/cm^2 at $1.45 \mu\text{m}$ and 7 ms (the lifetime of excited Er^{+3} in the

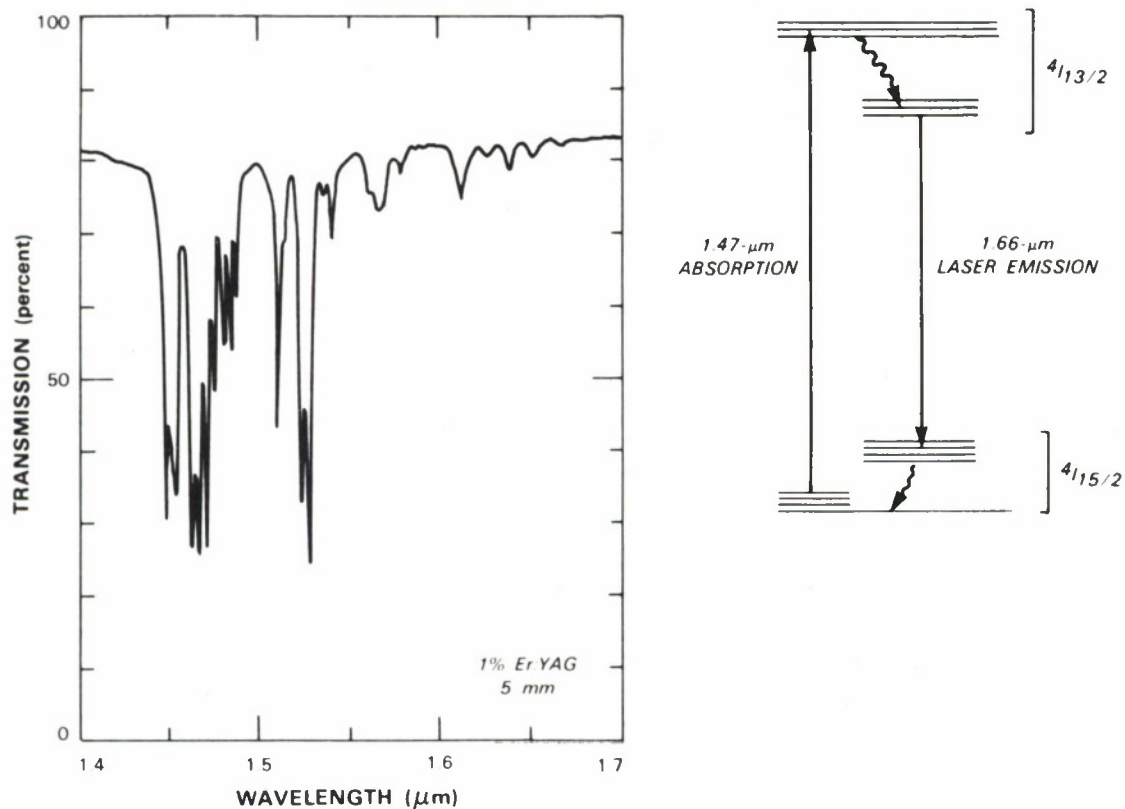


Figure 2-1. Spectroscopy of Er:YAG.

$^4I_{13/2}$ level) after the onset of pumping, the ratio of upper-to-lower-state population (N_u/N_l) was found to be 1.9 at 300 K and 10.4 at 195 K. The maximum energy extraction efficiency is given by $1 - (N_l/N_u)$; this yields extraction efficiencies of 47 percent at 300 K and 90 percent at 195 K. Single-pass gains are given by $G = \exp[(N_u - N_l)\sigma_L]$ and are 1.63 at 300 K and 12.2 at 195 K for a 10-cm path. These predicted gain values indicate that the diode-laser-pumped Er:YAG laser should operate with moderate pumping power. Further work is being conducted to verify these predictions.

D.K. Killinger

2.2 KTP FREQUENCY CONVERSION

A study of the feasibility of achieving high-efficiency tripling of 1.645- μ m laser radiation has been initiated. It is necessary that the tripling be performed at relatively high average-power levels with pulse lengths of the order of 100 μ s. Tripling is carried out in two steps; the first involves second-harmonic generation (SGH), and the second involves summing the fundamental and frequency-doubled beams.

The only commercially available nonlinear crystals which are potentially suitable for this application (i.e., transparent over the spectral range from 0.54 to 1.65 μ m) are LiNbO₃, LiIO₃, and KTiOPO₄ (KTP). LiNbO₃ has been eliminated from initial consideration because of the extreme temperature sensitivity of its indices of refraction, which tends to limit its power-handling capability, and the presence of two-photon absorption near the tripled frequency.¹ In addition, SHG experiments carried out under similar conditions have indicated that KTP has several advantages relative to LiIO₃, including a higher power-handling capability, a higher effective figure of merit, and a higher damage threshold.²⁻⁵ For these reasons, initial research efforts have been directed primarily toward further study of KTP.

KTP is an orthorhombic biaxial crystal with mm2 symmetry, with different indices of refraction (n_x , n_y , n_z) along each of the principal axes. Hence, the index of refraction along an arbitrary direction is a function of two angles, θ and ϕ , where θ is taken as the angle between the beam direction and the z-axis and ϕ is the angle between the x-axis and the x-y-plane component of the beam direction.

Using the Sellmeier equations for KTP (Reference 6) to determine the indices of refraction at the requisite frequencies, we have calculated the phase-matching angles, the effective nonlinear susceptibility (d_{eff}), and the angular and spectral bandwidths (FWHM) for doubling 1.645- μ m radiation and for summing 1.645- and 0.822- μ m radiation. The results are given in Table 2-1 and are compared with similar results reported for frequency-doubling 1.06 μ m. The values of θ and ϕ shown in Table 2-1 are those which maximize d_{eff} for the given frequency conversion. Only type II phase-matching results are given, because d_{eff} values obtained using type I phase matching are almost an order-of-magnitude smaller.

A notable feature of the 1.645- μ m doubling and summing relative to the 1.06- μ m doubling is the much larger walkoff angle ($>2.5^\circ$). This factor, coupled with the sharply reduced angular bandwidth, may severely limit the ability to achieve high-efficiency tripling starting with a single 1.645- μ m source.

<p style="text-align: center;">TABLE 2-1 Type II Frequency Conversion in KTP</p>			
	SHG 1.06 μm	SHG 1.645 μm	Summing 1.645 + 0.822 μm
θ (deg)	90 ^(a)	53.3	59
ϕ (deg)	26 ^(a)	0	0
d_{eff} (m/V)	7.4×10^{-12} ^(c)	6.1×10^{-12}	6.5×10^{-12}
Angular Bandwidth (mrad-cm)	15 to 68 ^(b)	1.7	0.9
Spectral Bandwidth (\AA -cm)	5.6 ^(b)	47	15
Walkoff (mrad)	4.5 ^(c)	47	48
<p>(a) Reference 2 (b) Reference 3 (c) Reference 4</p>			

The damage threshold of KTP when irradiated with a 15-ns laser pulse is 250 MW/cm², and SHG experiments at 1.06 μm with a 3.9-cm-long crystal have shown an initial efficiency slope of approximately 0.3%/MW (Reference 3). This is significantly below the efficiency value predicted on the basis of the standard SHG equation⁷ using the known d_{eff} value⁴ and assuming complete optical transmission and phase matching. The efficiency is proportional to $d_{\text{eff}}^2/\lambda^2 n^3$, where λ is the laser wavelength and n is the refractive index. Comparison of the values at 1.064 and 1.645 μm indicates that conversion efficiency at 1.645 μm should be down from that at 1.064 μm by a factor of over 3, assuming all other effects equal.

We have obtained a $3 \times 3 \times 5$ mm KTP crystal oriented for SHG phase matching at 1.645 μm . The crystal is being used in conjunction with relatively long laser pulses ($\sim 1 \mu\text{s}$) at 1.645 μm obtained from a pulsed, Q-switched Co:MgF₂ laser. Initial investigations will include optical absorption measurements between 0.5 and 2 μm , a damage threshold determination at the longer pulselength, and SHG conversion experiments.

N. Menyuk

REFERENCES

1. A.A. Kazukov, V.A. Konavalov, S.V. Shavkunov, and E.A. Shalaev, *Sov. J. Quantum Electron.* **13**, 1054 (1983).
2. Y.S. Liu, D. Dentz, and R. Belt, *Opt. Lett.* **9**, 76 (1984).
3. Y.S. Liu, L. Drafall, D. Dentz, and R. Belt, G.E. Techn. Inf. Series Rept. No. 82CRD016 (General Electric, Schenectady, New York, 1982).
4. J.Q. Yao and T.S. Fahlen, *J. Appl. Phys.* **55**, 65 (1984).
5. M.M. Choy and R.L. Byer, *Phys. Rev. B* **14**, 1693 (1976).
6. Airtron Corporation (private communication).
7. R.L. Byer, "Nonlinear Optical Phenomena and Materials," in *Annual Review of Materials Science*, Vol. 4, R.A. Huggins, R.H. Bube, and R.W. Roberts, Eds. (Annual Reviews Inc., Palo Alto, California, 1974).

3. MATERIALS RESEARCH

3.1 CMOS GATE ARRAYS AND DYNAMIC SHIFT REGISTERS FABRICATED IN ZONE-MELTING-RECRYSTALLIZED SOI FILMS

For some time, we have been using zone-melting recrystallization (ZMR) by the graphite-strip-heater technique to prepare Si-on-insulator (SOI) films on 3-in.-dia. Si wafers.¹ The films generally contain numerous subgrain boundaries (subboundaries) and, in some cases, surface imperfections such as protrusions and voids. For SOI wafers mounted on a vacuum chuck, after ZMR the total warp is less than 5 μm , peak to valley.²

To evaluate the ZMR SOI films for integrated-circuit applications, we measured the performance of CMOS test circuits fabricated in 3-in.-dia. films. To design the test chip incorporating these circuits, the design of a chip used in bulk CMOS process development was modified for SOI and silicon-on-sapphire (SOS) processing. The SOI/SOS chip, based on a 5- μm design rule, contains a 120-gate array, a two-phase dynamic shift register, and various test structures for process control and parameter testing. The chip size is about 6×6 mm. Fabrication is accomplished by a single-poly, single-metal process requiring a total of seven photolithographic masks.

Three 3-in. SOI wafers and three 3-in. commercial SOS wafers, each with a Si film 0.5 μm thick, were processed. Figure 3-1 is a photograph of a finished SOI wafer, which contains about 90 test chips. Figure 3-2(a) is a photograph of an SOI gate-array circuit, which consists of two ring oscillators with fanout of 1 and 3, respectively, and several NAND-gate delay chains. The circuit contains about 600 transistors. Figure 3-3(a) is a photograph of an SOI shift register.

Individual SOI n- and p-channel test devices show well-behaved characteristics with surface electron and hole mobilities of ~ 600 and $240 \text{ cm}^2/\text{V-s}$, respectively. The corresponding mobilities for the SOS devices are ~ 450 and $220 \text{ cm}^2/\text{V-s}$. Figure 3-2(b) shows typical output waveforms for the two ring oscillators in the SOI gate-array circuit. The waveforms show full voltage swing for a 5-V supply voltage. Figure 3-2(c) is a plot of stage delay vs supply voltage for the SOI, SOS, and bulk Si circuits. For a supply voltage of 5 V and a fanout of 1, the stage delay is 1.2 ns for the SOI circuit compared with 1.4 and 2 ns, respectively, for the SOS and bulk circuits. The higher speed of the SOI circuit is attributed to the higher carrier mobility and lower parasitic capacitance of the SOI devices. The yield of SOI gate-array circuits is approximately 60 percent. The inoperative circuits often contain visible surface defects, which are mostly voids in the SOI film. Reducing the density of such defects would lead to a significant improvement in circuit yield.

Selected SOI test chips were packaged for the measurement of dynamic shift register circuit performance. The measurements were made with a tester having a maximum clock frequency of 20 MHz. Figure 3-3(b) shows the performance at a clock frequency of 10 MHz. The circuit performs properly up to at least 20 MHz and down to 20 Hz. The high-speed performance is consistent with the low stage delay observed in the ring-oscillator measurements, and the low-frequency operation indicates low leakage current.

The present results show that the subboundaries in the ZMR SOI films do not significantly affect the performance of circuits with a 5- μm design rule, but surface imperfections such as voids are detrimental to circuit operation. Elimination of these imperfections is therefore necessary to permit the utilization of ZMR SOI films for large-scale integrated-circuit applications.

B-Y. Tsaur
C.K. Chen

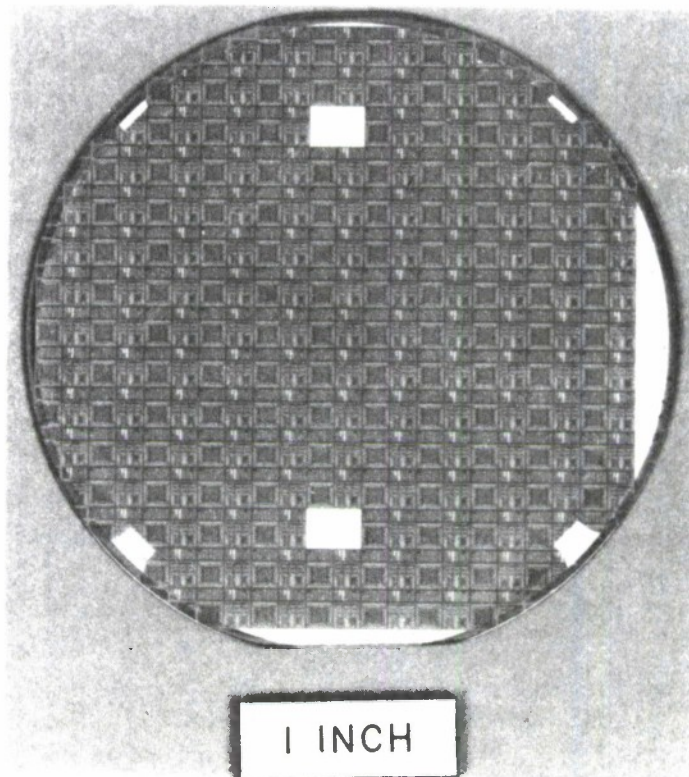


Figure 3-1. Photograph of a 3-in.-dia. SOI wafer after fabrication of CMOS test chips.

155596-N

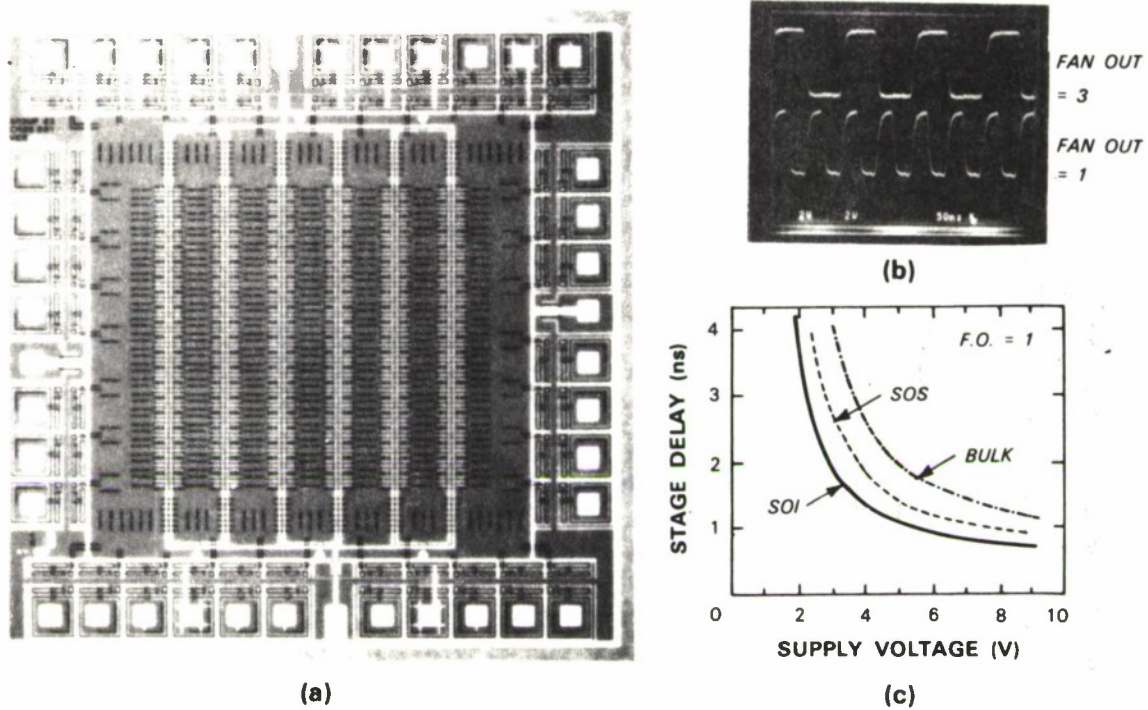


Figure 3-2. (a) Photograph of an SOI CMOS gate-array circuit. (b) Output waveforms of SOI ring oscillators with fanout of 1 or 3. (c) Ring oscillator stage delay as a function of supply voltage for SOI, SOS, and bulk Si gate-array circuits.

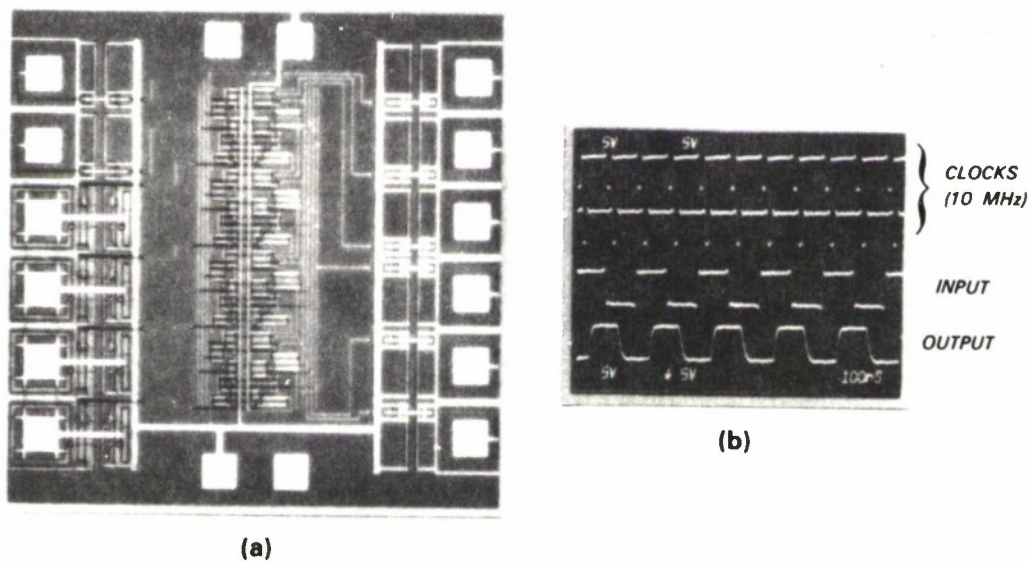


Figure 3-3. (a) Photograph of an SOI CMOS dynamic shift register. (b) Input and output waveforms of the shift register at a clock frequency of 10 MHz.

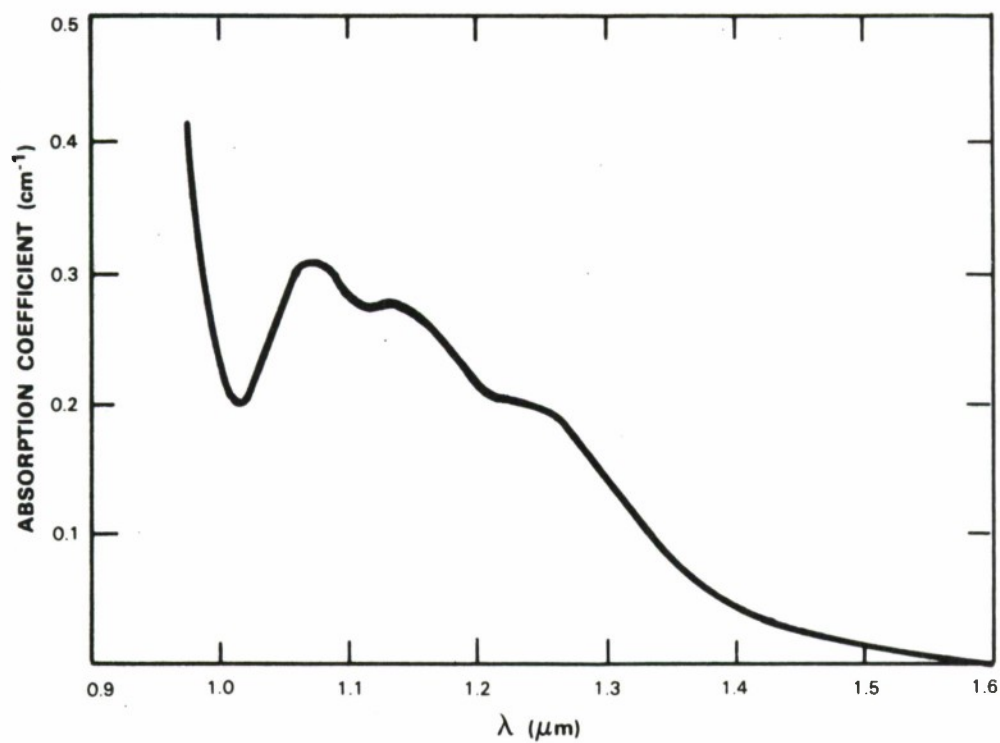


Figure 3-4. Optical absorption vs wavelength for an n-type InP sample doped with V, but not intentionally doped with any other impurity.

155599-N

3.2 OPTICAL AND ELECTRICAL PROPERTIES OF V-DOPED InP

An essential requirement for a viable InP-based microwave and millimeter-wave IC technology is the availability of high-quality, semi-insulating InP substrates with sufficient thermal stability to permit the fabrication of reproducible devices. Semi-insulating bulk InP crystals have so far been prepared only by doping with Fe or Cr, which typically yields resistivities of 10^7 to 10^8 and 10^4 to 10^5 Ω -cm, respectively. The thermal stability of substrates obtained from such crystals is marginal. Since the preparation of semi-insulating GaAs by means of V doping has recently been reported,^{3,4} we have carried out an investigation to determine whether V doping can also be used to prepare semi-insulating InP. Unfortunately, we have found that this is not the case.

Samples for optical and electrical measurements were cut from a number of InP boules grown by the liquid-encapsulated Czochralski technique from melts doped with 0.3 to 0.6 at.% V. In some growth runs, the V was added to the starting charge. In others, in order to demonstrate the effects of V doping as clearly as possible, the V was dropped into the melt after part of the boule had been grown, and samples were cut from the regions grown before and after the V was added. This delayed-doping procedure was used for growing one n-type boule and several p-type boules, using starting charges that were nominally undoped and lightly Zn doped, respectively. The last-to-freeze portion of every boule appeared to contain precipitated or occluded second-phase material, suggesting that the solubility limit for V may have been reached.

Figure 3-4 shows the room-temperature optical absorption spectrum measured from 1.0 to 1.6 μ m for a sample from the V-doped portion of the n-type boule grown by the delayed-doping procedure. The spectrum is similar to the one obtained for V-doped n-type InP by Zakharenkov *et al.*,⁵ who have attributed the observed absorption bands to intra-atomic transitions from the occupied ground state of the V center.

Figure 3-5 shows room-temperature absorption spectra for two samples from a p-type Zn-doped boule grown by the delayed-doping procedure. The lower, featureless curve was obtained for a sample from the portion of the boule grown before addition of V to the melt. The upper curve, which was measured for a sample from the region grown after V addition, shows the structure characteristic of absorption by the V center. The absorption bands are not much lower in intensity than those for the n-type sample of Figure 3-4, although they are somewhat broader. Since the V concentration in the n- and p-type samples should be comparable, this similarity in intensity implies that the degree of occupation of the V center is also similar. This, in turn, implies that the electronic level of V in InP cannot lie far above the position of the Fermi level in the p-type sample, which is located about 0.18 eV above the valence-band edge. For example, if the V level were located even 0.25 eV above the valence-band edge it would be only about 5-percent occupied in this sample, and the absorption would be much weaker. Thus, this level must lie lower than about 0.25 eV above the valence-band edge. Therefore, the level must be fully occupied in n-type samples, where the Fermi level lies close to the bottom of the conduction band.

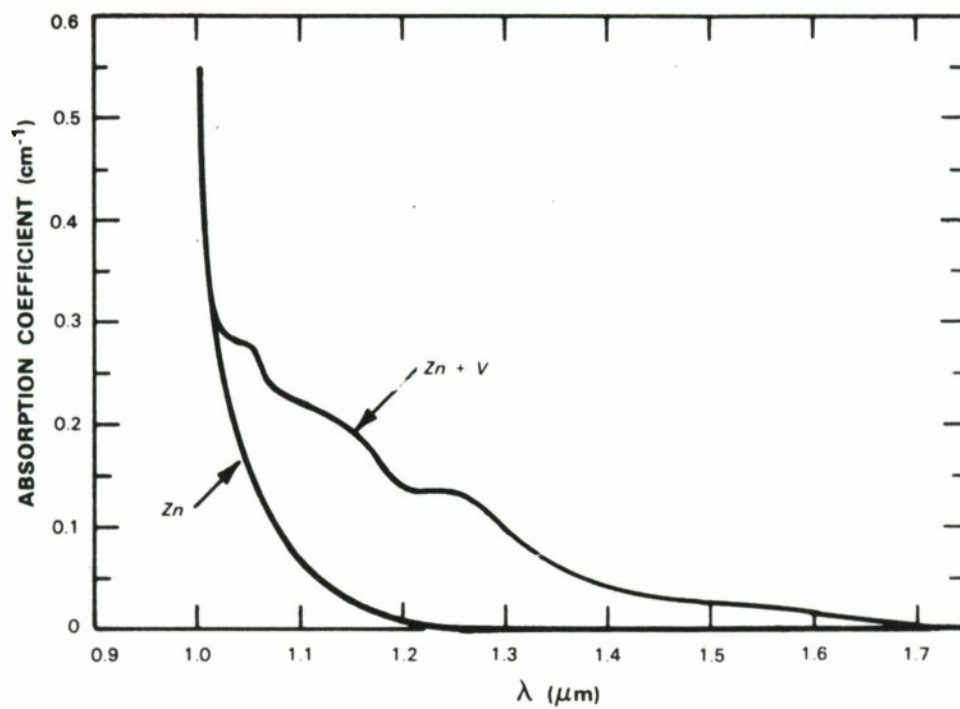


Figure 3-5. Optical absorption vs wavelength for regions of a Zn-doped, p-type InP crystal grown before and after addition of V to the melt.

155600-N

The optical absorption results establish that V is present in the portion of the InP boules grown after V is added to the melt, but they do not show whether V is electrically active in InP. To investigate this question, Hall-coefficient measurements were made to determine carrier concentration as a function of distance along the vertical axis of the n- and p-type boules grown by the delayed-doping procedure. In the p-type boule, the hole concentration varies smoothly from about $5 \times 10^{15} \text{ cm}^{-3}$ at the bottom to about $3 \times 10^{15} \text{ cm}^{-3}$ at the top. If V is electrically active, it changes the carrier concentrations in this boule by significantly less than 10^{15} cm^{-3} . The results for the n-type boule are plotted in Figure 3-6. Although the electron concentration increases appreciably after the addition of V to the melt, it is unlikely that this increase is due to the donor action of V, since a donor located close to the valence-band edge would not be expected to make a significant contribution to the electron concentration in a material containing shallow donors. The observed increase might be due to the normal segregation of residual electrically active impurities, the introduction of a donor impurity as a contaminant in the V, or a change produced by V in the gettering action⁶ of the B_2O_3 encapsulant.

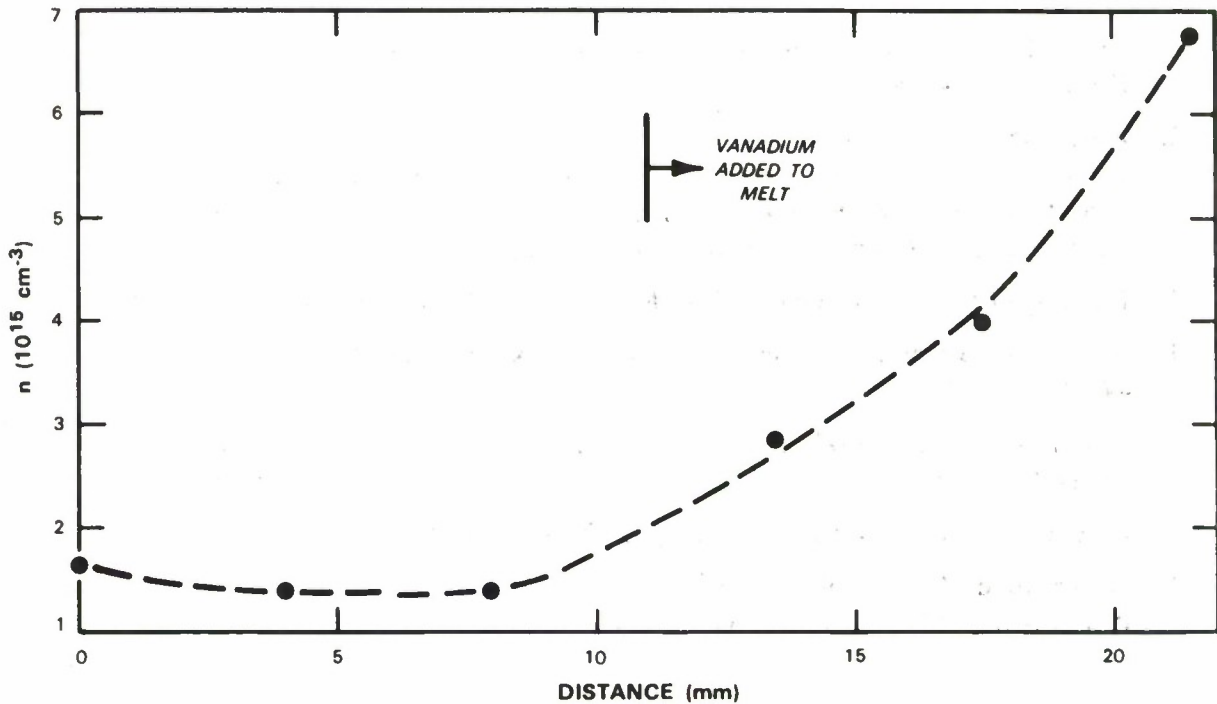


Figure 3-6. Carrier concentration vs distance along the vertical axis for an n-type InP crystal initially grown without intentional doping, and then doped with V.

On the basis of deep-level optical spectroscopy and secondary-ion mass spectrometry (SIMS) data, Bremond *et al.*⁷ have concluded that V is a donor in InP which is located about 0.2 eV above the valence-band edge and has a maximum concentration in the mid- 10^{15} cm⁻³ range. This assignment is consistent with our data, since such a donor would not significantly compensate the Zn acceptors in p-type material with a hole concentration of only 3 to 5×10^{15} cm⁻³.

Our results do not establish whether or not V is electrically active in InP. They do show, however, that the V level must lie lower than about 0.25 eV above the valence-band edge. Therefore, V doping cannot be used to obtain semi-insulating InP, since the preparation of such material requires the use of a level closer to the center of the forbidden band.

G.W. Iseler

REFERENCES

1. J.C.C. Fan, B-Y. Tsaur, and M.W. Geis, *J. Cryst. Growth* **63**, 453 (1983), DTIC AD-A147189.
2. C.K. Chen, M.W. Geis, H.K. Choi, B-Y. Tsaur, and J.C.C. Fan, in *Energy Beam-Solid Interactions and Transient Thermal Processing 1984*, edited by D.K. Biegelsen, G.A. Rozgonyi, and C.V. Shank, Materials Research Society Symposium, Vol. 35 (Materials Research Society, Pittsburgh, Pennsylvania, 1985), p. 613.
3. M. Akiyama, Y. Kwarada, and K. Kaminishi, *J. Cryst. Growth* **68**, 39 (1984).
4. K. Kütt, D. Bimberg, M. Maier, H. Kräutle, F. Köhl, and E. Bauser, *Appl. Phys. Lett.* **44**, 1078 (1984).
5. L. Zakharenkov, Y. Mal'tsev, V. Masterov, and L. Pasechnik, *Sov. Phys. Semicond.* **17**, 1409 (1983).
6. E. Kubota and A. Katsui, *Jpn. J. Appl. Phys.* **24**, L344 (1985).
7. G. Bremond, A. Nouailhat, G. Guillot, B. Deveaud, B. Lambert, Y. Toudic, B. Clerjaud, and C. Naud (unpublished).

4. MICROELECTRONICS

4.1 S-BAND MODELING OF A PLANAR MILLIMETER-WAVE RECEPTOR

The development of planar heterodyne receiver circuits operating at short-millimeter and submillimeter wavelengths can be accelerated if the S-parameters of the circuits can be estimated. Because direct measurements at these frequencies are either difficult or impossible, scale-model measurements of these parameters have been made on one circuit which has shown promise as an element in a millimeter-wave imaging array.¹

The circuit investigated contains a pair of full-wavelength microstrip dipole antennas spaced by $\lambda/2$, which feed a GaAs Schottky diode located midway between the two dipoles. The circuit was modeled at 3.2 GHz using copper tape of 100- μm thickness as the conductor and Stycast* K3.8 as the dielectric. The S-parameter measurements were made with a vector network analyzer, which excited the circuit at the diode port via a coaxial feed. No mixing diode was present in the model circuit.

An estimate of S_{11} is important for improving the match between the antenna structure and the mixing element. With the use of a GaAs Schottky diode, the feed should present the diode with an impedance of approximately 200 ohms for best mixer sensitivity.² An SIS device, which has also been used as the nonlinear element in this circuit, generally requires a lower impedance for the best performance.³

Figure 4-1 shows the impedance measured through a $\lambda/4$ balun for the model circuit near resonance. The values of impedance suggest that an alteration to the millimeter-wave-circuit design could improve the match between the antenna and the Schottky diode. One possible change is an increase in the feed gap of the dipole antenna. This holds promise because increasing the feed gap of a full-wavelength dipole antenna generally decreases its resistance. This reduced resistance is transformed to a higher resistance at the diode port by the $\lambda/4$ transmission line between each antenna and the diode port. The impedance at the diode port may also be changed by altering the lengths of the $\lambda/4$ transmission lines. Additional measurements need to be made to evaluate the effect of these changes and to determine the influence, if any, of the balun used in the model circuit.

When the circuits are spaced closely on the same substrate, as required for an imaging array, a measurement of $|S_{12}|$ allows channel isolation to be determined. The coupling between adjacent circuits is caused by near-field radiation as well as the propagation of surface waves along the dielectric substrate.⁴ $|S_{12}|$ was measured in the E- and H-plane configurations with receptor separation of λ_0 in each case, as shown in Figure 4-2. The results given in the figure lead us to believe that the close element spacing necessary for diffraction-limited imaging ($\sim\lambda_0$) at millimeter wavelengths will provide a high degree of channel isolation.

J.A. Taylor
W.J. Piacentini

* Emerson and Cuming Corporation, Canton, Massachusetts.

$$Z_1 = 41 + j64 \, \Omega$$

$$f_1 = 3.10 \, \text{GHz}$$

$$Z_2 = 38 + j23 \, \Omega$$

$$f_2 = 3.25 \, \text{GHz}$$

$$Z_3 = 88 + j57 \, \Omega$$

$$f_3 = 3.65 \, \text{GHz}$$

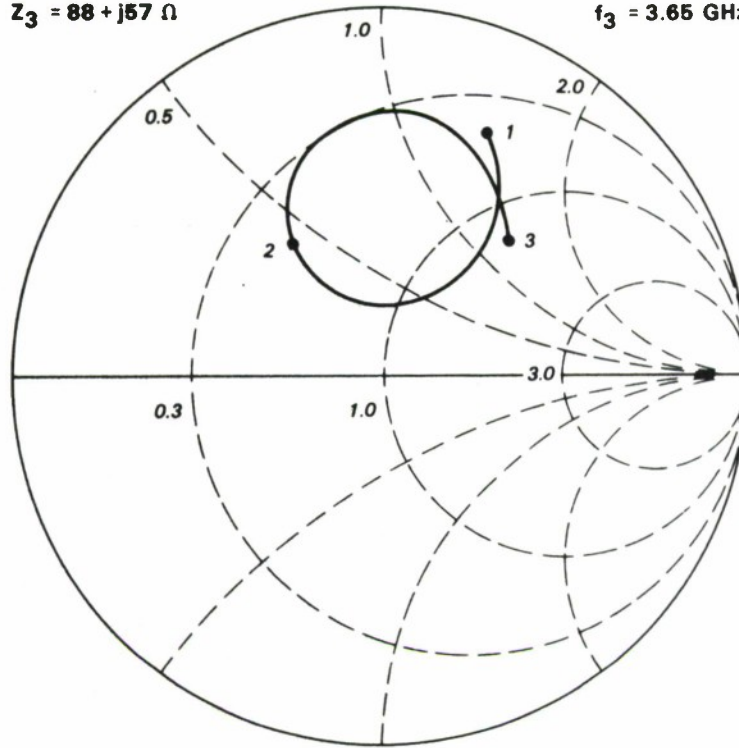


Figure 4-1. Smith chart display of impedance of single receptor when excited at diode port near resonance.

155615-N

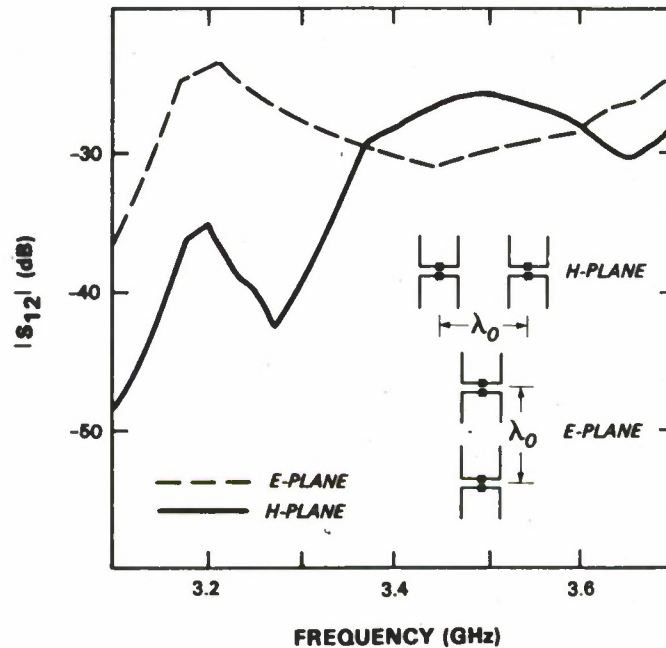


Figure 4-2. $|S_{12}|$ between two receptors spaced by λ_0 in the E- and H-plane configurations.

4.2 REPRODUCIBLE MICROWAVE PERFORMANCE OF GaAs PERMEABLE BASE TRANSISTORS

Reproducible fabrication of high-frequency permeable base transistors (PBTs) with maximum stable power gains as high as 20.7 and 14.1 dB at 18 and 26.5 GHz, respectively, have been observed. The large, reproducible power gains of these devices exceed the microwave performance of all PBTs fabricated to date.

A particularly good PBT wafer was fabricated approximately three years ago using chloride-transport vapor phase epitaxy (VPE) for the overgrowth of the W base grating. This wafer contained a number of devices having an extrapolated maximum frequency of oscillation (f_{\max}) exceeding 100 GHz (Reference 5). Numerous VPE-overgrown PBT wafers have been fabricated in the years since, but this result could not be duplicated. To better understand the factors affecting VPE overgrowth for PBTs, a comprehensive set of diagnostic experiments using secondary-ion-mass-spectrometry (SIMS) analysis was conducted on PBTs overgrown using both VPE and organometallic chemical-vapor deposition (OMCVD). The chemicals involved in the OMCVD epitaxial process were found not to incorporate in the overgrown GaAs, as happens with Cl in the VPE process^{6,7}; therefore, PBTs were fabricated using Se-doped OMCVD overgrowth. The results on this first wafer were very encouraging, with the exception of the output impedance, which was significantly lower for the Se-doped OMCVD-overgrown PBT wafer compared with the best VPE-overgrown PBT wafer.^{7,8} This low output impedance reduces the extrapolated f_{\max} but does not significantly affect the unity short-circuit current gain frequency f_T .

SIMS analysis done on this PBT and other test PBTs indicates that during the OMCVD overgrowth a large and uncontrollable enhanced incorporation of Se occurred in the GaAs grown over W gratings, compared with epitaxial growth on a homogeneous GaAs surface. This enhanced dopant incorporation was responsible for the low output impedance. Si then was used as the dopant during the OMCVD overgrowth of a PBT, and no enhanced incorporation of Si near the W gratings was observed from the SIMS analysis; therefore, Si would appear to be a superior dopant for PBT overgrowths. PBTs were then fabricated using Si-doped OMCVD overgrowth of the W base gratings. This PBT wafer duplicated the microwave performance of the best VPE-overgrown PBT wafer.⁹

In spite of the encouraging results obtained with OMCVD overgrowth, contamination introduced by pre-overgrowth processes remained as a source of variability in PBT wafers. These contaminants can produce an uncontrolled carrier concentration in the grating region and can increase electron scattering, preventing ballistic transport. Consequently, a major effort was undertaken to improve the purity of the W and the cleanliness of the pre-overgrowth processing. The concentrations of Cu, Cr, and Au were significantly reduced in the sputter-deposited W by cleaning the sputtering system and dedicating it to high-purity W. Also, the purity of the Ni RIE mask was improved by cleaning the electron-beam evaporation system before the Ni was deposited. Dedication of the plasma asher to pre-overgrowth PBT fabrication eliminated gold contamination from this source, and pre-etching the asher chamber eliminated Mg, Si, Ti, Cr, and Fe contamination. Improved wafer-handling techniques, such as dedicated vacuum wands and tweezers, reduced environmental contamination in the PBT.

All the above procedures then were used to make a new set of PBT wafers which were grown in both horizontal and vertical OMCVD systems using Si doping. The scattering parameters of these wafers were obtained in a network analyzer from 0.1 to 26.5 GHz. The calculated maximum stable power gains for two PBT wafers, one overgrown in a vertical OMCVD system (HiP2) and another overgrown in a horizontal OMCVD system (Hp2), are shown in Figure 4-3. HiP2 has good microwave performance up to 18 GHz; however, above this frequency the bonding wires used to connect the collector and base to the test fixture produce resonances which degrade the accuracy of the network analyzer measurements. Extrapolation of the maximum stable power gain for this PBT from 18 GHz, using -6-dB/octave roll-off, yields an f_{\max} of 195 GHz. This PBT has a power gain of 20.7 dB at 18 GHz, which is the highest power gain at this frequency of any PBT fabricated to date.

To eliminate these parasitic resonances, gold mesh was used to bond the collector and base contacts to the test fixture. The microwave performance of Hp2 under optimized bias conditions for maximum power gain at 26.5 GHz is shown in Figure 4-3. Under these conditions the extrapolated f_{\max} for this PBT wafer, grown in a horizontal OMCVD system, is 150 GHz. This device also has the highest power gain at 26.5 GHz (14.1 dB) of any PBT fabricated to date.

Table 4-1 shows a summary of the microwave characteristics encompassing all the devices processed in this most recent set of wafers. Six of the eight PBT wafers have an f_{\max} exceeding 100 GHz. This improvement in average performance and reproducibility compared with earlier PBT wafers is quite encouraging. The other two devices were grown together, side by side, in the

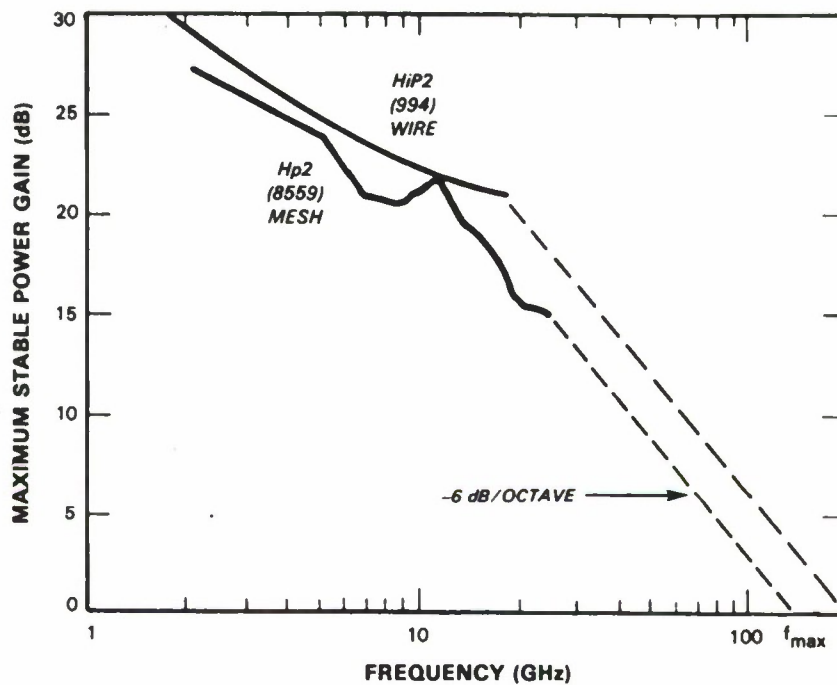


Figure 4-3. Maximum stable power gain for two PBTs fabricated using Si-doped OMCVD overgrowth.

TABLE 4-1					
Comparison of Microwave Characteristics of Si-Doped, OMCVD-Overgrown, GaAs PBTs					
PBT Wafer	OMCVD System		Maximum Stable Power Gain (dB)		f_{\max} (GHz)
	Run	Type	18 GHz	26.5 GHz	
HiP1	993	Vertical	16.8	12.5	125
HiP2	994	Vertical	20.7	—	195
Vic1	994	Vertical	15.2	12.4	110
HdB4	8559	Horizontal	16.8	12.1	125
Hp2	8559	Horizontal	18.5	14.1	150
HdB3	8558	Horizontal	Au Contamination	—	—
Hp4	8558	Horizontal	12.3	10.3	86
Hp3	8557	Horizontal	15.0	—	102

same OMCVD overgrowth deposition. SIMS analysis on HdB3 indicates that this wafer was contaminated with gold. How it was contaminated is unknown. However, this wafer may have cross-contaminated Hp4 in the OMCVD system or during the pre-overgrowth cleaning, which may account for the extrapolated f_{\max} of only 80 GHz obtained with the latter wafer.

In summary, incorporation of impurities in the PBT has been reduced by improving the purity of the sputtered W and by using extremely clean pre-overgrowth processing. When these procedures are used, high reproducibility of PBTs with an extrapolated f_{\max} exceeding 100 GHz has been obtained. While the contamination control instituted to date has been quite effective, significant levels of contaminants are still present. Thus, further reduction of these contaminants should improve the reproducibility and the performance of the PBT even more.

K.B. Nichols	R.A. Murphy
M.A. Hollis	S. Rabe
C.O. Bozler	A. Vera
R.P. Gale	W.J. Piacentini

4.3 SPECTRAL MEASUREMENT OF QUANTUM WELL WIDTH

A photoluminescence technique can be used to determine quantum well widths in GaAs-AlGaAs superlattices or single wells, as described below. This method is convenient and accurate within the limits imposed by theoretical calculations. We expect it to be more reliable than the empirical determination of the quantum well widths by using the crystal-growth-rate data in an MBE system.

In photoluminescence at low temperatures in quantum well structures, one observes a well-resolved exciton emission consisting of light and heavy hole lines. The energy separation between these two lines consists of the splitting due to quantum well confinement and the difference in the excitonic binding energies of the light and the heavy hole. Both of these energies are dependent on the quantum well width L , although the quantum well confinement splitting is more sensitive to L than the exciton energies. With a theoretical scheme to calculate the energy separation between these two exciton states, an effective value of L can be determined from analyzing photoluminescence data.

In a theoretical approach by Jiang,¹⁰ the two aspects of the problem (quantum well confinement and excitonic effect) are decoupled. This is achieved by using a variational-perturbation method in which the Coulomb interaction is approximated by a two-dimensional form. This reduces the problem to that of a system with two decoupled modes of motions — parallel and perpendicular to the plane of the quantum well. Jiang also simplifies the problem by treating the heavy and light holes as different particles with scalar masses. This assumption introduces significant error in the confinement energies only in narrow quantum wells (<80 Å), where the penetration of the particle wavefunction into the barrier (AlGaAs) is appreciable. On the other hand, the approach is shown to produce accurate exciton binding energies, and to provide a physically valid model for a two-dimensional exciton.¹¹

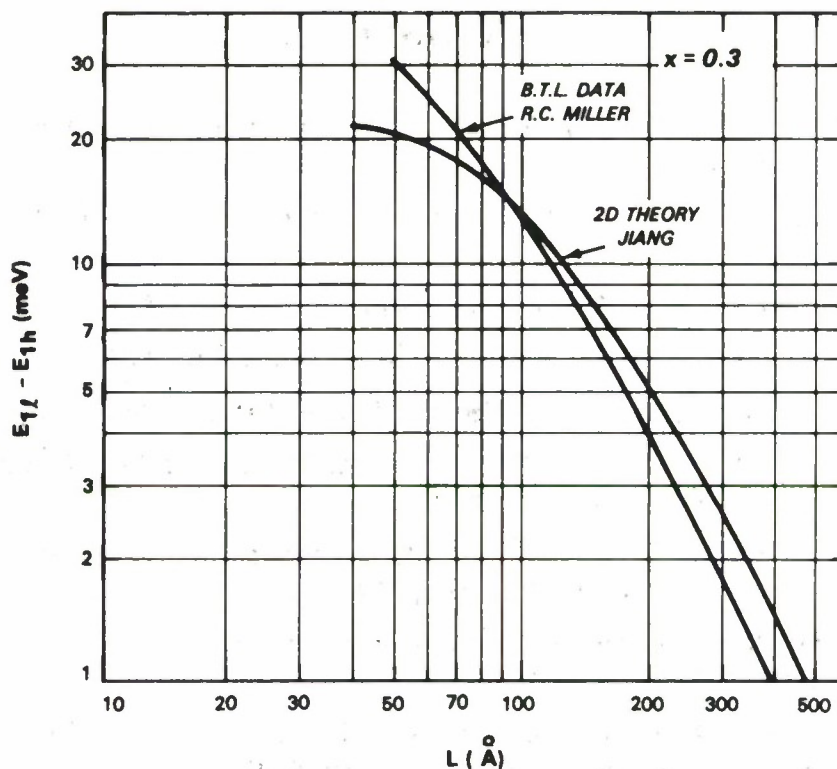


Figure 4-4. Energy separation between light- and heavy-hole exciton emission in $Ga_{1-x}Al_xAs$ quantum wells.

Using the physical parameters for GaAs and AlGaAs,¹² we plot the result of the calculation of the exciton splitting from the above theoretical approach, and compare it with the experimental values by Miller *et al.*¹³ The values of quantum well widths reported in Reference 13 are determined by using the crystal growth rate and the times of growth, and are estimated to be about 10-percent uncertain. The discrepancy between the two curves shown in Figure 4-4 can be resolved with a lateral shift of Miller *et al.*'s result from the theoretical result, which is consistent with the quoted figure of uncertainty in the former. We contend that the theoretical result from the two-dimensional model provides a reliable means of determining the quantum well width from photoluminescence data. This method can be further refined by taking into account the proper effective mass tensor representation of the valence band, dispensing with the notions of light and heavy holes as separate particles. The refined method will be more accurate and will be useful even in narrower quantum well structures. We propose to calibrate the theory to accurate measurements of quantum well widths determined from RHEED oscillations for values of L from 40 to 200 Å, where the scalar effective mass theory is valid.

B. Lax
H.Q. Le

REFERENCES

1. Solid State Research Report, Lincoln Laboratory, M.I.T. (1984:3), p. 70, DTIC AD-A154783.
2. D.E. Held and A.R. Kerr, IEEE Trans. Microwave Theory Tech. **MTT-26**, 55 (1978).
3. D.P. Woody *et al.*, IEEE Trans. Microwave Theory Tech. **MTT-33**, 90 (1985).
4. D.M. Pozar, IEEE Trans. Antennas Propag. **AP-31**, 740 (1983).
5. G.D. Alley *et al.*, IEEE Trans. Electron. Devices **ED-29**, 1708 (1982).
6. M.A. Hollis, K.B. Nichols, C.O. Bozler, A.R. Calawa, and M.J. Manfra, Prog. 1984 Electronic Materials Conf. (1984).
7. K.B. Nichols, R.P. Gale, M.A. Hollis, G.A. Lincoln, and C.O. Bozler, IEEE Trans. Electron. Devices **ED-31**, 1969 (1984).
8. Solid State Research Report, Lincoln Laboratory, M.I.T. (1984:3), p. 57, DTIC AD-A154783.
9. C.O. Bozler, M.A. Hollis, K.B. Nichols, S. Rabe, A. Vera, and C.L. Chen, to be published in IEEE Electron. Device Lett. **EDL-9** (1985).
10. T.F. Jiang, Solid State Commun. **50**, 589 (1984).
11. H.Q. Le, B. Lax, P. Maki, and L. Eastman (to be published).
12. R.L. Greene and K.K. Bajaj, Solid State Commun. **45**, 831 (1983).
13. R.C. Miller, D.A. Kleinman, and A.C. Gossard, Phys. Rev. B **24**, 7085 (1984).

5. ANALOG DEVICE TECHNOLOGY

5.1 THIN STRIPLINE DIELECTRICS WITH PASSIVATED SUPERCONDUCTORS

The signal-processing capability of analog signal-processing devices depends on, among other factors, the storage time of the devices. Superconducting analog signal-processing devices make use of electromagnetic delay lines as the storage element. Thus, it is desirable in these devices to be able to fabricate long delay lines in a compact structure. In order to pack a line densely without excessive undesirable coupling between adjacent segments of the line, it is necessary to use dielectrics as thin as $10\text{ }\mu\text{m}$. Described below is a technique for fabricating thin robust dielectrics incorporating chemically passivated superconducting thin-film ground planes.

The method for fabricating thin dielectrics reported previously¹ makes use of a heavily doped silicon wafer on which a lightly doped epilayer is grown. The epilayer side of the wafer is metalized to provide a ground plane and bonded to a glass substrate (Pyrex) using electrostatic bonding at 400°C (Reference 2). The original substrate is chemically dissolved by a resistivity-selective etch,³ leaving behind the epilayer upon which the delay-line conductor is deposited and patterned (Figure 5-1). Through stringent cleanliness and careful etch monitoring, large-area (4.8-cm-dia.) defect-free films as thin as $15\text{ }\mu\text{m}$ and uniform to less than $1\text{ }\mu\text{m}$ have recently been produced in our laboratory.

Resonators with a single Nb layer for the ground plane were built using this process in order to evaluate RF losses of the Nb metal and the Si dielectric. The quality factor Q of these resonators was too small to be measured. Two causes could be responsible for this: (1) the dielectric losses on the epilayer could be too high, or (2) the bonding process could be affecting the quality of the Nb ground plane.

Experiments were performed to investigate the problem. Non-epitaxial silicon wafers with known, low RF losses were bonded to glass and used for the fabrication of resonators. These resonators also had unmeasurably low Q s. Thus, the problem seemed to be associated with the deterioration of the Nb during bonding. This was confirmed both by DC measurements of the films and by the Auger profile of the structure. For the resistivity measurement, a structure consisting of patterned Nb strips on silicon was built. The resistivity ratio, $R(300\text{ K})/R(77\text{ K})$, of these strips was found to be higher than 2.5, indicating Nb of good quality. The silicon substrate was then electrostatically bonded to a glass substrate at 400°C in an N_2 atmosphere with the Nb strips at the bonding interface. Measurements of the resistivity ratio after the bonding showed a drop to approximately 1. Measurements at liquid helium temperatures confirmed the fact that the Nb was not superconductive at 4.2 K. Auger results [Figure 5-2(a)] show that a large amount of oxygen had diffused from the glass into the niobium.

To prevent the oxygen diffusion, we decided to investigate the use of NbN as a diffusion barrier. Nitrides are known to be good diffusion barriers because of the decoration of the grain boundaries with nitrogen, which prevents intergranular diffusion. Since the Auger results also showed that some diffusion of silicon into the 3000-Å-thick Nb film had occurred, 400-Å-thick

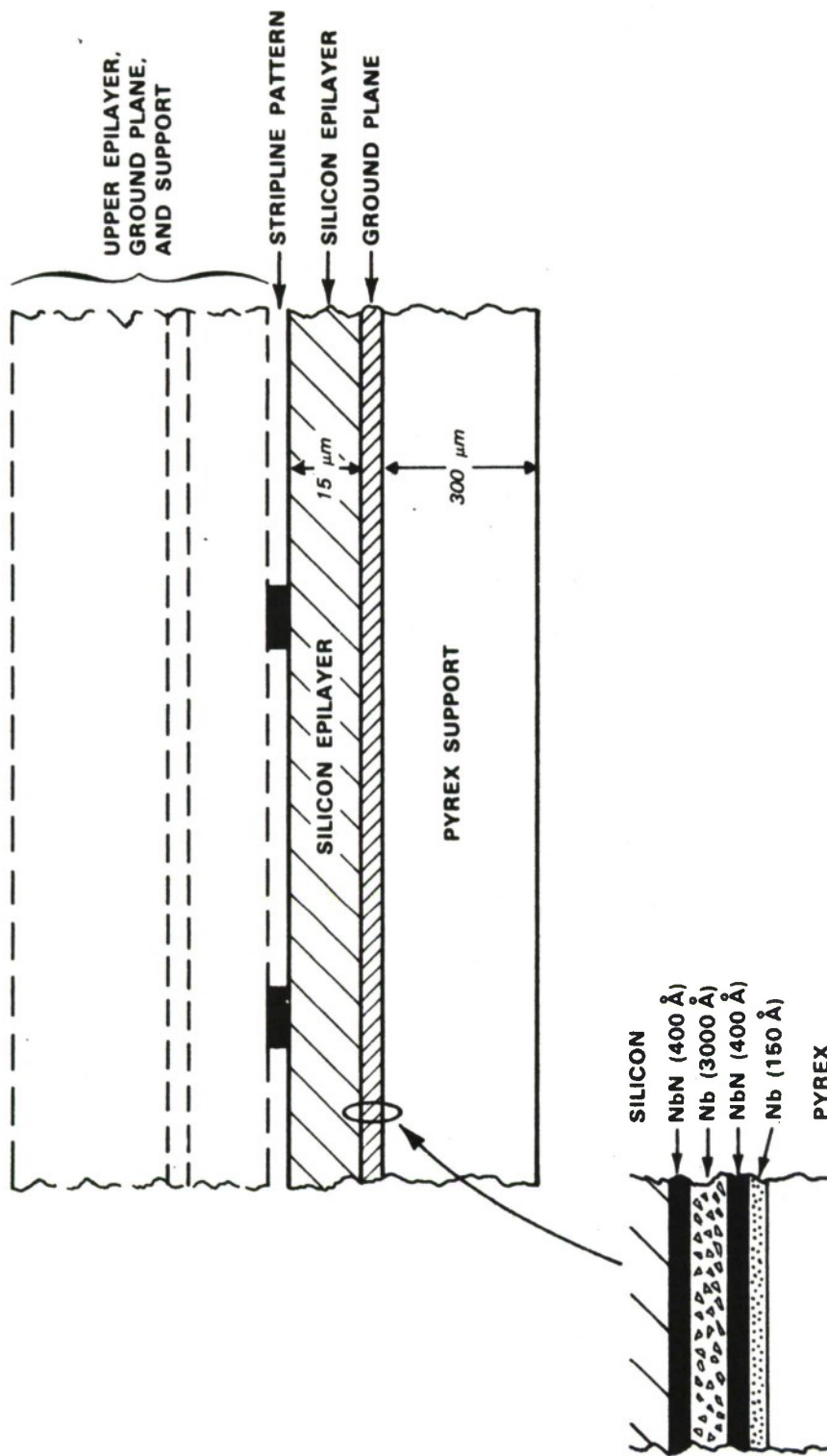


Figure 5-1. Cross section of a superconductive stripline delay line on bonded and etched silicon epilayers. The inset shows the passivated ground plane.

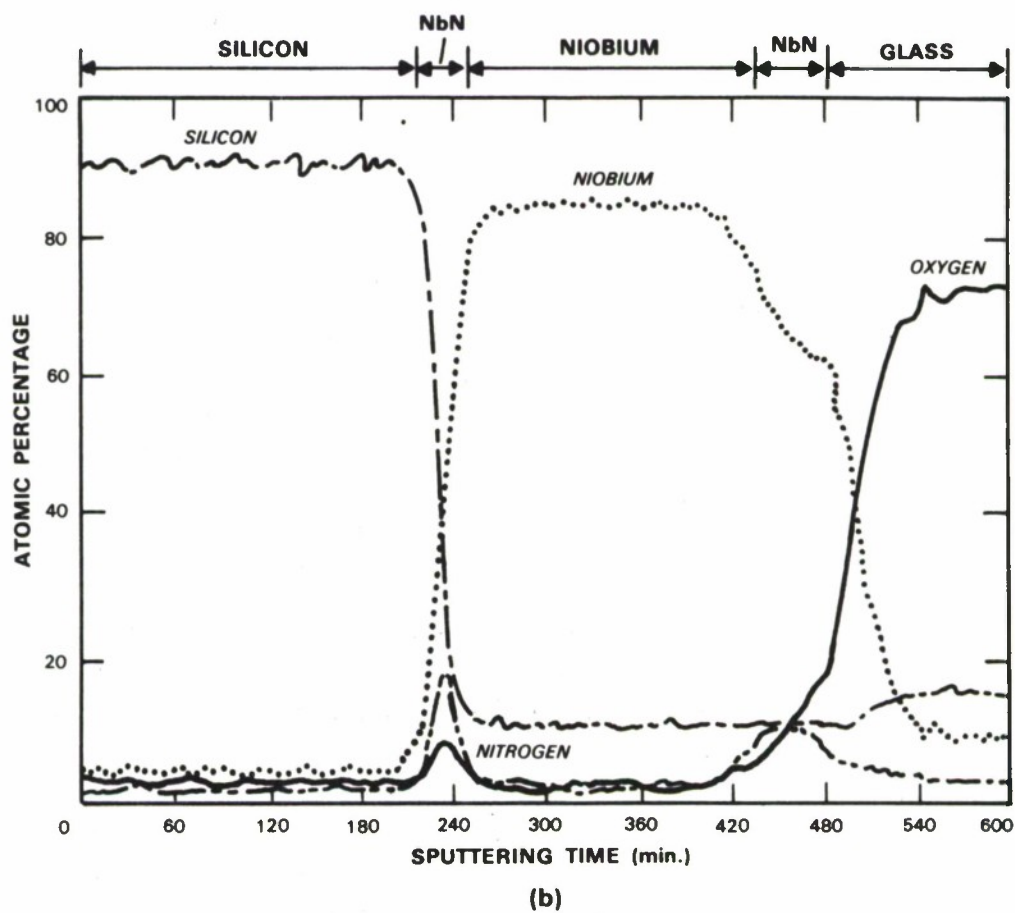
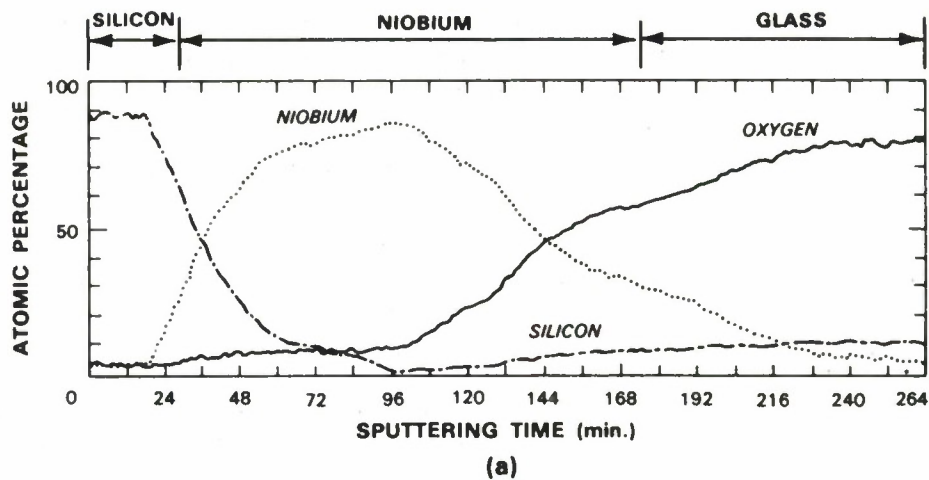


Figure 5-2. Auger profile of superconducting ground planes after bonding to Pyrex: (a) Nb ground plane; (b) NbN (400 Å)/Nb (3000 Å)/NbN (400 Å)/Nb (150 Å) ground plane. The high background level of silicon is an artifact of the high ion-beam current used to profile this sample.

NbN was used on both sides of the Nb layer. A thinner (150-Å) second layer of Nb had to be added onto the glass side of the multilayer structure to improve adhesion to the glass. This structure, shown in the inset of Figure 5-1, could be easily fabricated by alternatively introducing a partial pressure of nitrogen during sputter deposition of the niobium. DC conductivity measurements showed the films to be superconductive at 4.2 K after the bonding process. The Auger profile of Figure 5-2(b) shows clearly that both the oxygen and silicon diffusion was prevented. Using these films as ground planes, we fabricated test resonators on thin (30-μm) epilayer dielectrics. High Qs (290,000) at 562 MHz were obtained for these films, showing that losses in both the dielectric and the films are very low. Fabrication of delay lines with 2.6-GHz bandwidth and 220 ns of dispersion on 15-μm-thick dielectrics is under way.

NbN is a high- T_c superconductor, having low RF losses⁴ when deposited under the right conditions. We intend to substitute for the present structure a simpler one using high-quality NbN as a ground plane.

A.C. Anderson

J.A. Marden

R.S. Withers

5.2 BULK-ACOUSTIC-WAVE REFLECTIONS FROM OPTICALLY GENERATED HOLOGRAPHIC GRATINGS

We previously introduced the concept of holographic-grating acoustic-wave devices⁵⁻⁷ that are based upon the interaction of bulk acoustic waves (BAW) with an optically generated hologram. Such devices have the potential of operating over bandwidths of several gigahertz with delay times of tens of microseconds, an order-of-magnitude improvement in bandwidth over surface-acoustic-wave (SAW) devices. The basic device concept is shown in Figure 5-3, illustrated by the example of a simple filter structure. The grating in the bulk is made by the optical holographic technique of interfering two coherent light beams in the medium.⁸ The grating interacts with an acoustic wave by the electroacoustic effect by which an electric field causes changes in the acoustic velocity.^{6,9} In the simplest case, a periodic grating serves as a narrowband reflector of the acoustic wave. The light beams are used only to create the grating. Once the grating is established and the light is turned off, the grating remains and the device continues to function as a bandpass filter. The hologram can be erased by illuminating the crystal with a uniform beam of light. The grating can be made insensitive to light by fixing techniques which have been reported.⁸

We previously reported direct measurements of the electroacoustic coefficients in LiNbO_3 and LiTaO_3 for Z-propagating longitudinal waves.⁶ The measured values indicated that a strong acoustic reflector could be fabricated in both materials. The experimental vehicle that we used to measure the reflection of BAW from optically generated holograms is similar to the device pictured in Figure 5-3, except that a single transducer was used to launch and to detect the wave and the holographic grating filled the sample. To observe the reflections, a burst of acoustic energy at the Bragg frequency was launched in the crystal and reflected from the grating and the

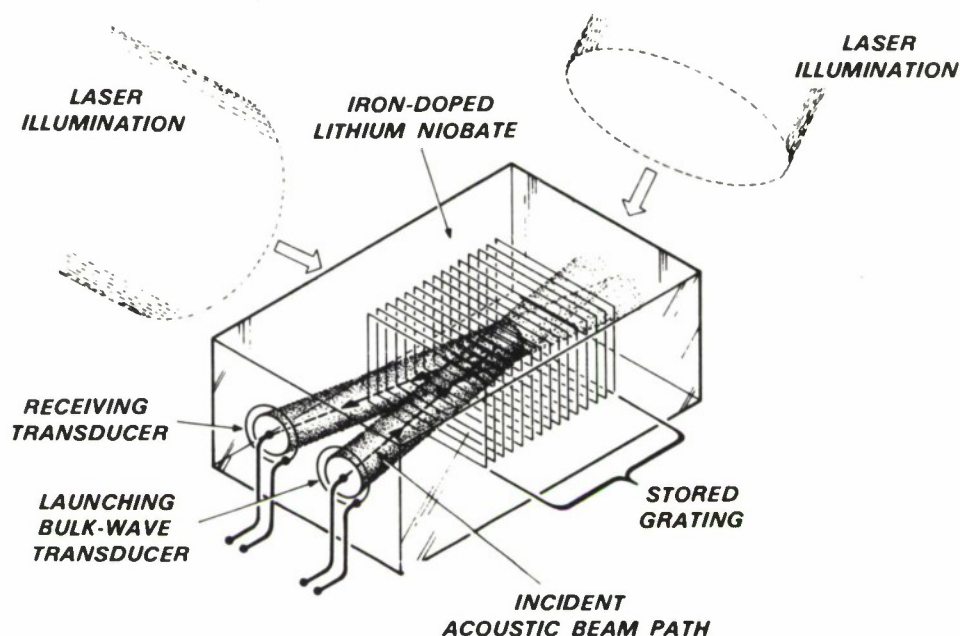
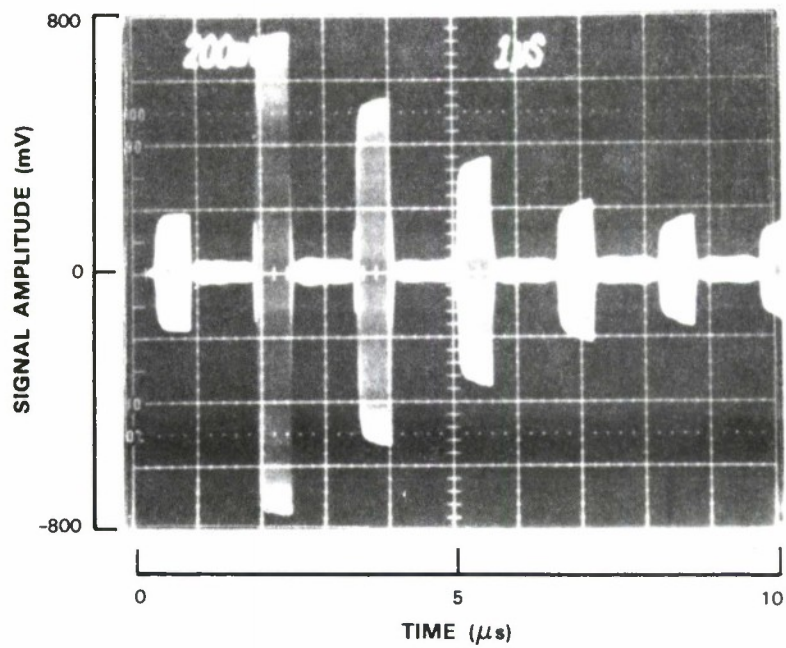


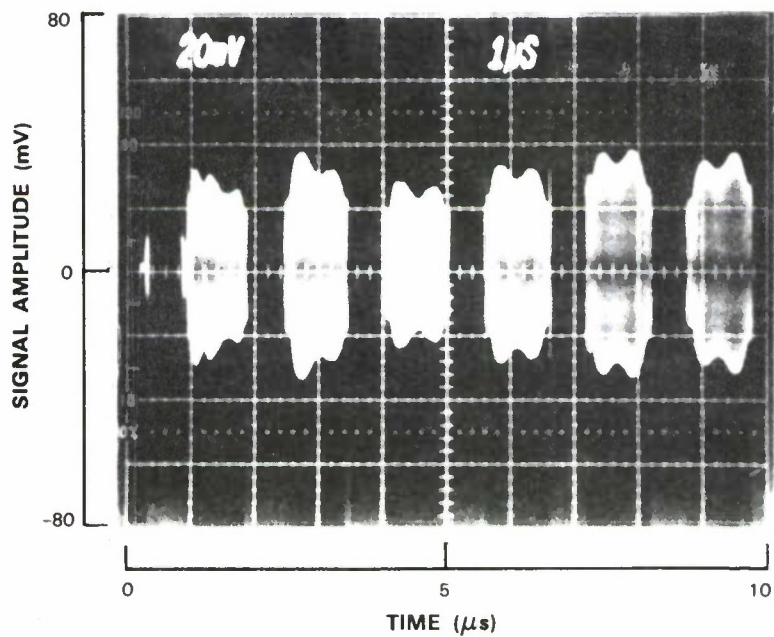
Figure 5-3. A simple BAW device, a bandpass filter. The stored grating is created by the laser illumination. The grating interacts strongly with the incident acoustic beam and reflects the energy contained in a narrow frequency band, thus forming a bandpass filter.

back face. The reflection from the grating returned to the input transducer before the reflection from the back face and the two reflections could be resolved in time. The experiments used samples of LiNbO_3 doped with 0.015% by weight Fe. A LiNbO_3 compressional-wave transducer was bonded to the Z face of the samples. The transducer was then lapped and polished for a fundamental resonance frequency of 300 MHz, with third overtone near 900 MHz. The face of the crystal opposite the bulk-wave transducer was polished flat and parallel to the transducer face, so that waves once launched would make many reflections whose decay rate would be determined by propagation loss and deviation from parallelism of front and back faces.

An optical hologram was written into the crystal using the 4658-Å line of an Ar laser. The resulting grating period was about $3.6 \mu\text{m}$, determined by the angle between the reference and the object beams. Figure 5-4(a) shows the result of launching a 400-ns-long burst of acoustic energy at 889 MHz, with corresponding acoustic wavelength of $\lambda_a = 7.2 \mu\text{m}$. The photograph shows first the attenuated electrical reflection from the transducer impedance mismatch, followed by six reflections from the back face of the sample. The decay of the reflections is due to attenuation and misalignment as discussed above. Figure 5-4(b) shows the same trace with a factor-of-10 larger gain. The electrical reflection of the input pulse and the reflections of the acoustic wave from the back face of the crystal are off scale in Figure 5-4(b) and thus not visible. The envelope of the reflections from the hologram is clearly visible, filling the spaces between the reflections from the back face. Each pass of the wave through the device produces a reflection from the



(a)



(b)

Figure 5-4. (a) Photograph of multiple reflections of an acoustic wave from back face of sample. A single transducer was used for both input and output. (b) Same as (a) but with 10 times larger gain. The reflections from the back face are off scale and not visible. The spaces between back-face reflections are filled with the reflection from the hologram.

hologram stored in the crystal. The variation in reflection amplitudes shown in the figure can be explained by slight misalignments of the initial acoustic beam, the faces of the crystal, and the planes of the hologram. Over time longer than that shown, the envelope of the reflections decays exponentially as expected. The hologram reflection shown in Figure 5-4(b) is about 30 dB lower than the reflection from the back face. Taking into consideration that the input pulse does not fully fill the sample, this implies a reflection coefficient per grating element of about 1.5×10^{-4} , which compares favorably with our earlier estimate⁶ of 2.7×10^{-4} .

To erase the holograms, the crystal is placed in the uniform illumination of only the reference beam. Over a period of six months, which has been our longest observation time, we noticed no decay of the hologram if it was left in the dark.

We have demonstrated the basis for practical filters that use the reflections of BAW from holographically created gratings. The reflection coefficient is large enough to envision a variety of wideband, high-performance filters or high-frequency resonators which are simple to fabricate and have great flexibility.

D.E. Oates
P.G. Gottschalk

5.3 EDGE DETECTION BY CONVOLUTION WITH A GAUSSIAN SCREEN

The difference-of-Gaussians (DOG) algorithm^{10,11} is being used increasingly for edge detection in image-processing applications. The computationally intensive step in this algorithm is the convolution of the image with each of a pair of Gaussian functions. In a previous report,¹² we described a method for producing these convolutions in a charge-coupled device (CCD) by the use of a novel clocking technique. We will describe below a simple system, based on classical optics, that performs the convolution of an image with arbitrary positive, space-limited functions, and we will then give the results of some edge-detection experiments obtained with the new method.

The idea that one can convolve two functions using geometrical optics is not new.¹³ However, the technique we have invented to vary the scale factor of the convolution kernel has not been described before. With previous techniques, one had to use different transparencies for each convolution kernel and maintain close registration between the transparencies. Moreover, the DOG algorithm requires convolutions with Gaussian functions having precisely the same integrated transmissivity. This would be especially difficult with conventional optical convolution techniques but, as will be seen, is automatic with ours.

A simplified setup which illustrates the basic principles is shown schematically in Figure 5-5. It consists of an object of intensity $I(x,y)$, a lens of focal length f , a screen with a transmissivity $T(x,y)$ placed adjacent to the lens, and a TV camera. The system operates as follows. If the image detector in the camera is in the image plane, then every point in the object maps into a point in the image, and the only effect of the screen is to reduce the effective aperture of the lens. However, if the image detector is moved a distance Δz out of the image plane, then what

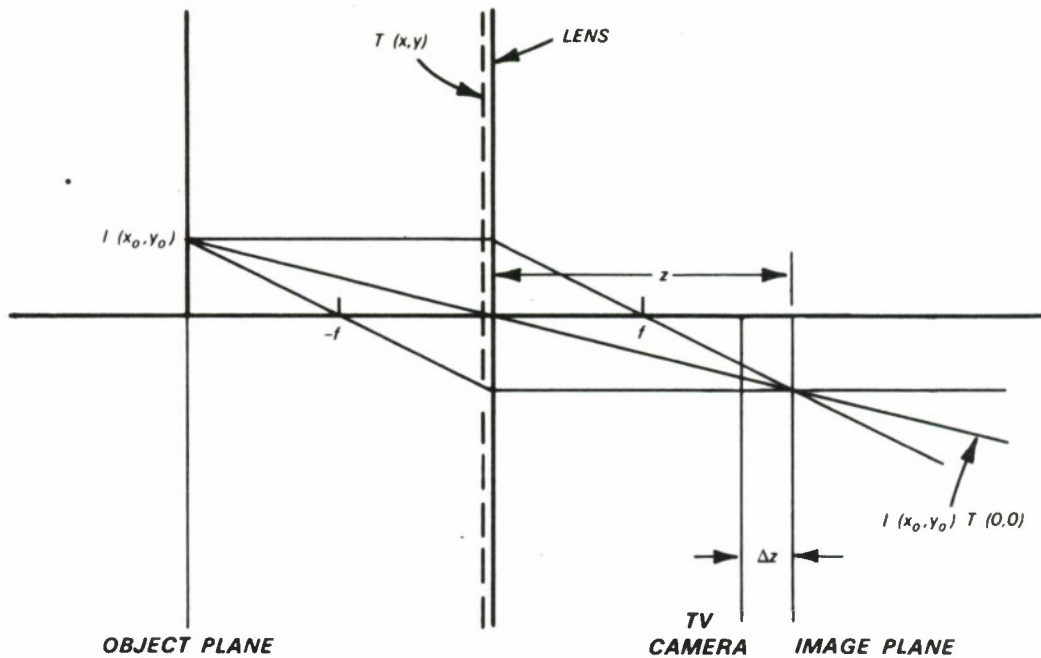


Figure 5-5. Schematic of a setup to obtain the convolution of an image with an arbitrary positive function. The scale of the kernel function is changed by moving the camera along the optical axis.

used to be a point in the image plane becomes a small replica of the screen $T(x,y)$ scaled by a factor

$$a = (\Delta z)/z$$

where z is the distance from the lens to the image plane. Thus, the transmissivity pattern of the screen becomes the point-spread function of the imaging system, and, therefore, the light intensity distribution in the plane of the imager is the convolution of the normal sharp image with this minified replica of the screen. By varying Δz one can generate convolutions of the object with a range of kernel functions all having the shape of the screen, but with varying scale factors. Since the light is only redistributed, the total intensity in the point-spread function is constant. This is perfect for carrying out the DOG algorithm.

However, there is one problem with the convolutions produced using the setup shown in Figure 5-5. When the camera is moved, not only does each spot of light turn into the point-spread function described above, but there is also a shift in the center position of the point-spread function. The entire image suffers a scale change. This means that two Gaussians generated for DOG cannot be subtracted without first performing a scale transformation on one or both of them.

This problem is overcome with the modified apparatus shown in Figure 5-6. We place the center of the Gaussian screen on the optical axis at a distance f from the lens. With this arrangement, the rays that pass through the center of the screen come out parallel to the optic axis, and we can move the position of the camera without affecting the magnification of the image.

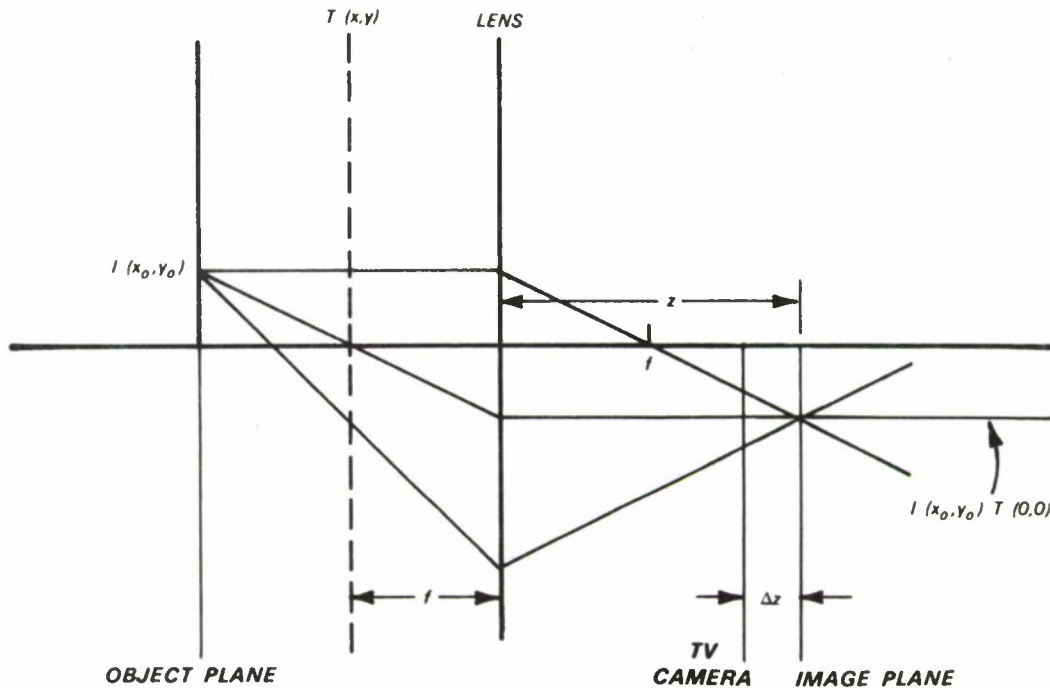
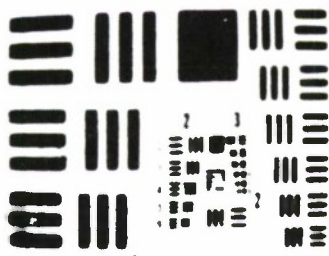


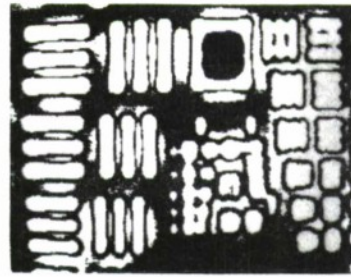
Figure 5-6. Modified arrangement for optical convolution. The center of the screen is placed on the optical axis at a distance f from the lens. With this arrangement, the scale of the kernel function can be varied without changing the magnification of the image.

To demonstrate the usefulness of our setup for edge detection, we made a screen with a Gaussian transmission pattern and performed the convolution of a resolution chart with Gaussian functions of different widths. These images were digitized and stored in a computer, where pairs corresponding to Gaussian width parameters in a 2:1 ratio were subtracted. Zero crossings of the difference were detected and displayed on a monitor. Figure 5-7 shows (a) the original sharp image of the resolution chart, (b) the result of edge extraction using optical Gaussian convolutions, and (c) the result using computer-calculated Gaussian convolutions of the sharp image. Except for a higher noise level owing to noise in the TV camera, our optical convolver has performed correctly.

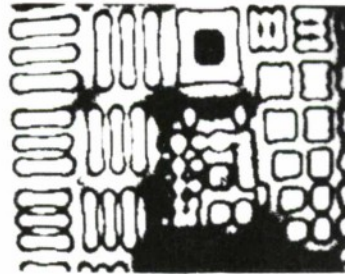
The convolution technique described here could be used as the basis for a special edge-detection camera. Stepping motors or piezoelectric positioners should be able to carry out the small physical motions required (typically in the millimeter range) in less than the frame time of the camera. Gaussian or other convolutions would be carried out virtually instantaneously, and, since they are performed in the optical domain, there are no errors resulting from either amplitude or spatial quantization. Size and power requirements would be modest. Two limitations of the optical convolution technique should be kept in mind. First, since the Gaussian filtering is done before image detection, noise generated in the camera is not filtered, as it is in a post-detection convolver. Second, since only one convolution is carried out at a time, the scene under



(a)



(b)



(c)

Figure 5-7. (a) Original focused image used for the DOG. (b) Results of the edge extraction using optical Gaussian convolutions. (c) Results of edge extraction using computer-calculated Gaussian convolutions of the original picture.

155610-N

study must not move significantly (on the order of the Gaussian widths) in the time necessary to record the two convolved images.

A.L. Lattes
J.P. Sage

5.4 FAST WIDEBAND PHASE-LOCKED LOOP FOR NARROWBAND EXCISION

Wideband receivers are vulnerable to narrowband interference, whether friendly or hostile. Any signal which exceeds the desired signal will capture the automatic gain control (AGC) and thus suppress the desired signal. Signal-processing algorithms have been developed by Arsenault¹⁴ to suppress the larger of two signals, the near/far case in a network environment. A more severe situation exists in the case of co-located systems. In a tactical environment, wideband systems

may be co-located with narrowband systems. In some cases, these systems may even share the same antenna mast. Narrowband systems cope with this situation by partitioning the frequency band and providing adequate EMI and RFI shielding. These techniques can provide up to 100 dB of in-band interference rejection, whereas the wideband systems depend solely on processing gain. However, if the interference saturates the receiver front end, there could be little signal remaining to process.

In most receivers the system dynamic range is limited by the first amplifier stage, because a large interference will saturate the input stage. In saturation, the output of this amplifier may actually be lower than the input (i.e., negative gain) which, when added to the small-signal suppression effect,¹⁴ could easily push the desired signal well below the noise floor. In the system under development, the unwanted signal is excised prior to any nonlinear stages, and thus the signal-to-noise ratio is preserved within 2 dB of the input. The excision is achieved by replication of the unwanted interference and subtraction from the original signal.

Figure 5-8 is a block diagram of the exciser. A sample of the receiver input is provided by the 20-dB input coupler to an amplifier/limiter chain. The limiter-chain output is a constant-amplitude square wave at the frequency of the largest input, thus suppressing all other signals as in an FM receiver. This output is then used to lock a phase-locked loop (PLL) which generates a pure spectral line at the interfering frequency. This signal is then coupled back to the input via a voltage-controlled attenuator, a phase shifter, and amplifiers for subtraction from the original waveform. A sample of the remainder after subtraction is fed back to determine the residue and adjust the amplitude and phase of the replicated interference needed to minimize the residue.

The performance of the system is determined by how quickly and how accurately the interference may be replicated. The goal was a 30-dB cancellation; this somewhat arbitrary level was chosen as both useful and achievable. This level requires an amplitude accuracy of 0.2 dB and a phase accuracy of 1.3° . Speed is equally important, because many of the possible co-located systems will be frequency hoppers, requiring that the system be capable of setting to the new frequency as quickly as possible. A maximum set-on time of 20 μ s was chosen as a goal, again as something both usable and achievable. Achievement of this speed and accuracy requires superlative performance in the PLL. Therefore, the primary emphasis of this program has been on the development of the PLL.

Figure 5-9 is a block diagram of PLL. There are three loops, the first of which is a frequency discriminator which sets the voltage controlled oscillator (VCO) nominally on frequency and reduces the static phase error when the loop is in phase lock. With the other two loops disabled, the frequency discriminator will keep the VCO within 1.5 MHz across the 100-MHz band. The static phase error is reduced from 30° to 3° across the band with this loop. The second loop is a frequency-difference discriminator which generates an error voltage proportional to the difference frequency of the VCO and the signal. This acts as an accelerator to aid in phase lock. The third loop is the phase-locked loop which, together with the difference-frequency discriminator, forms a "quadrice correlator" (References 15 and 16). All three loops operate with a closed-loop bandwidth of 10 MHz to speed acquisition and minimize settling time. This is somewhat contrary

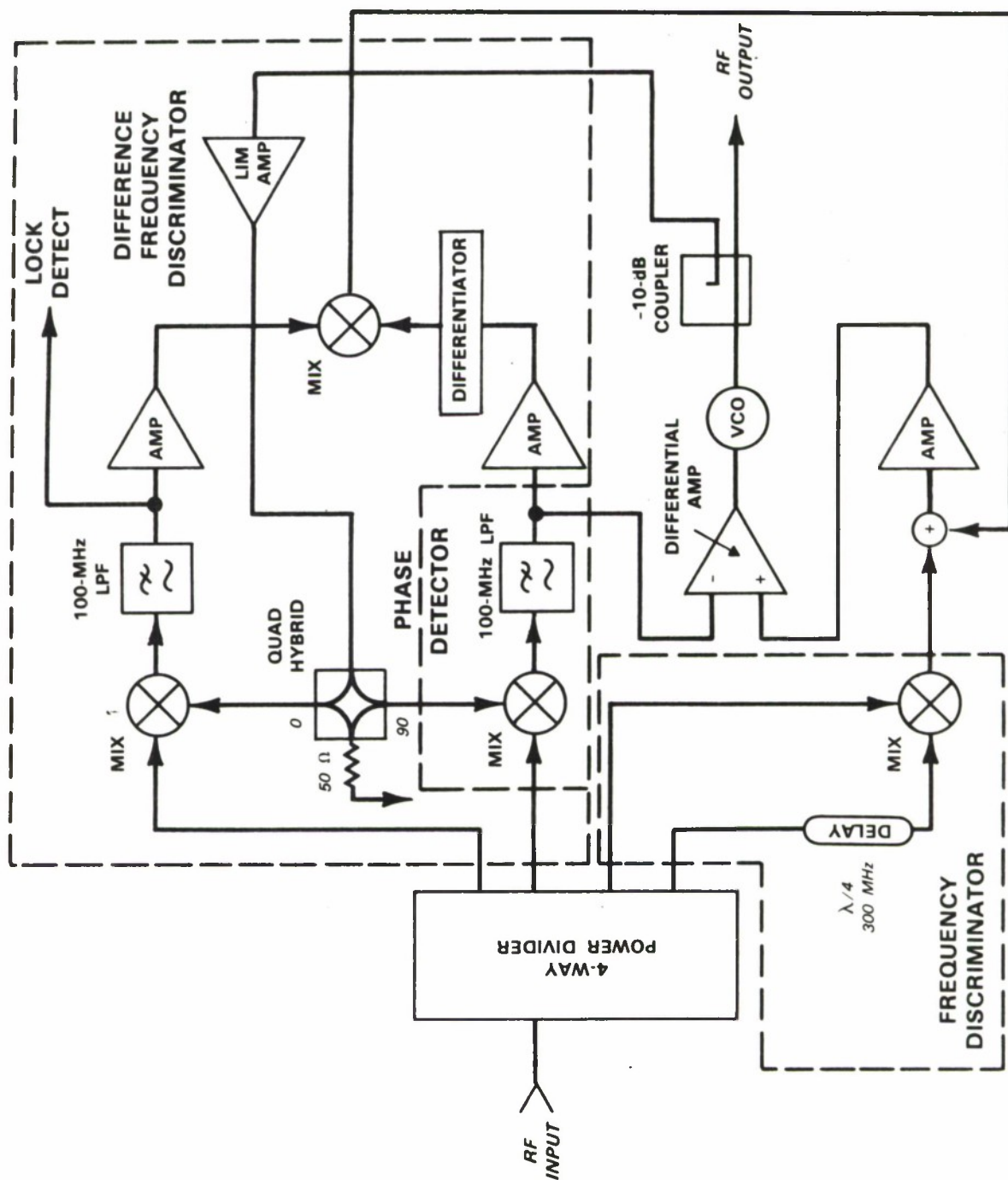


Figure 5-9. Phase-locked loop.

to conventional PLL design, where the object is to track weak signals in a noisy environment. In that case, the object is to make the closed-loop bandwidth as small as possible.

The design of the PLL has been completed and a final prototype assembled and tested. Figure 5-10 is a spectrum of the PLL output when locked to a CW signal. This spectrum shows that the spurious output, measured over any 10-kHz-wide band, is 55 dB down in the near-in sidelobes and that the remaining sidelobes are virtually nonexistent. From this spectrum, the total spurious power integrated over the 100-MHz band is estimated to be 40 dB below the carrier. Figure 5-11(a) is a waveform taken from the voltage output of the phase detector as the input frequency is stepped from 250 to 350 MHz. The flat portion of the waveform represents the time when the loop is in lock. Note that the time to lock is less than 20 μ s. The peak-to-peak amplitude when the loop is out of lock represents the peak phase error, i.e., 180° or approximately 30° per division. This shows variation in the static phase error to be 3° or less in this worst case. Figure 5-11(b) is a step of 10 MHz, from 340 to 350 MHz. The time to lock in this case is greatly reduced, as is the static error. Both the lock time and the static error are linearly proportional to the frequency step.

The design has been reduced to a 4- by 6-in. multilayer stripline circuit board that will be integrated with the rest of the excision circuitry.

G.T. Flynn
K.R. Bennett

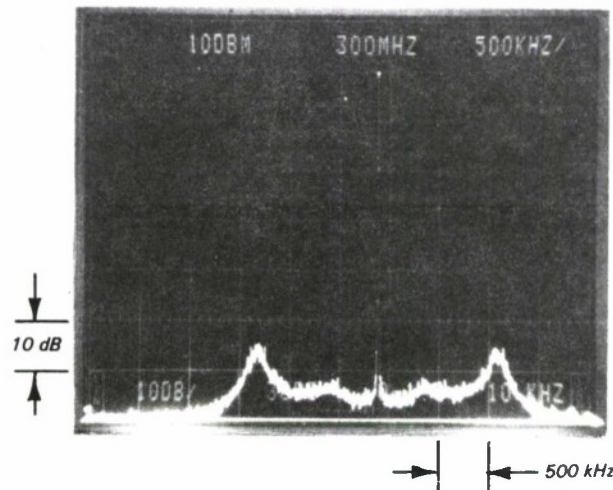


Figure 5-10. Phase-locked-loop output spectrum. Note that a 10-kHz measurement bandwidth is used.

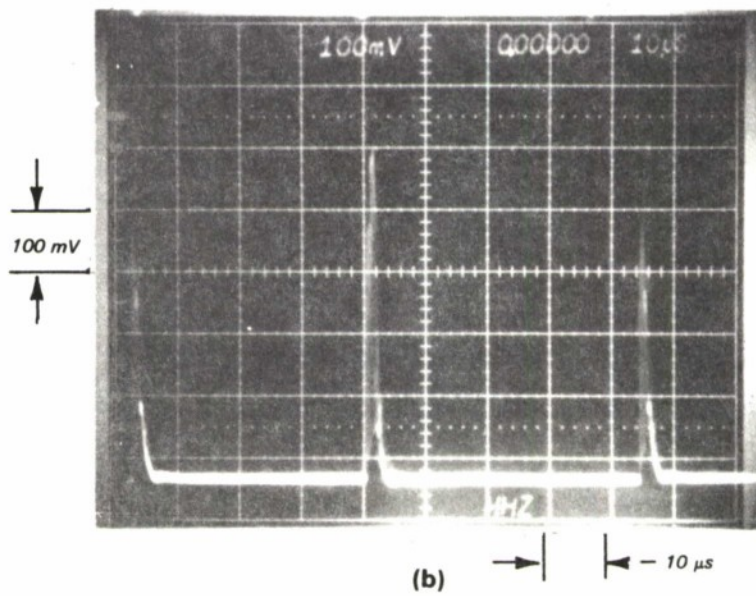
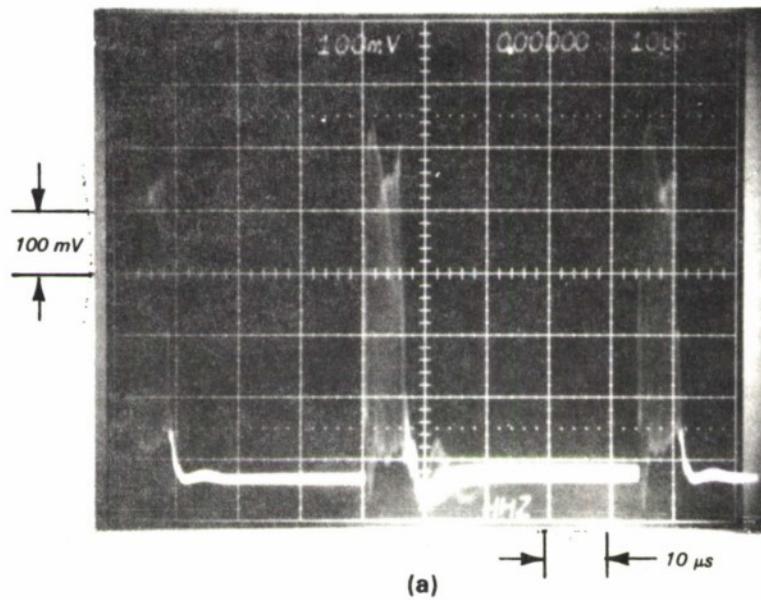


Figure 5-11. Phase error response to an (a) 100-MHz frequency step, and (b) 10-MHz frequency step.

REFERENCES

1. Solid State Research Report, Lincoln Laboratory, M.I.T. (1983:2), p. 55, DTIC AD-A134594.
2. G. Wallis, *Electrocomp. Sci. Tech.* **1**, 45 (1975).
3. H. Muraoka, T. Ohhashi, and Y. Sumitomo, in *Semiconductor Silicon 1973*, H.R. Huff and R.R. Burgess, Eds. (Electrochemical Society, Princeton, New Jersey, 1973), p. 327.
4. Solid State Research Report, Lincoln Laboratory, M.I.T. (1985:2), pp. 37-41.
5. *Ibid.* (1984:1), p. 73, DTIC AD-A147429.
6. P.G. Gottschalk, D.E. Oates, and P.V. Wright, *1983 Ultrasonics Symposium Proceedings* (IEEE, New York, 1983), p. 1091, DTIC AD-A147595.
7. Solid State Research Report, Lincoln Laboratory, M.I.T. (1984:2), p. 68, DTIC AD-A147640.
8. D.L. Stabler, in *Topics in Applied Physics Vol. 20, Holographic Recording Materials*, H.M. Smith, Ed. (Springer-Verlag, Berlin, 1977), p. 101.
9. B.H. Agishev, V.V. Lemonov, and N.K. Yushin, *Sov. Phys. Solid State* **20**, 1629 (1978).
10. D. Marr and E.C. Hildreth, *Proc. R. Soc. London* **B270**, 187 (1980).
11. D. Marr, *Vision* (V.H. Freeman, San Francisco, 1982).
12. Solid State Research Report, Lincoln Laboratory, M.I.T. (1983:4), p. 53, DTIC AD-A142991.
13. M.A. Monahan, K. Bromley, and R.P. Bocker, *Proc. IEEE* **65**, 121 (1977).
14. Solid State Research Report, Lincoln Laboratory, M.I.T. (1984:4), pp. 47-52, DTIC AD-A158013.
15. F.M. Gardner, *Phaselock Techniques* (Wiley, New York, 1979), pp. 86-87.
16. D. Richman, *Proc. IRE* **42**, 106 (1954).

UNCLASSIFIED

SECURITY CLASSIFICATION OF THIS PAGE (When Data Entered)

REPORT DOCUMENTATION PAGE		READ INSTRUCTIONS BEFORE COMPLETING FORM
1. REPORT NUMBER ESD-TR-85-241	2. GOVT ACCESSION NO.	3. RECIPIENT'S CATALOG NUMBER
4. TITLE (and Subtitle) Solid State Research		5. TYPE OF REPORT & PERIOD COVERED Quarterly Technical Report 1 May — 31 July 1985
		6. PERFORMING ORG. REPORT NUMBER 1985:3
7. AUTHOR(s) Alan L. McWhorter		8. CONTRACT OR GRANT NUMBER(s) F19628-85-C-0002
9. PERFORMING ORGANIZATION NAME AND ADDRESS Lincoln Laboratory, M.I.T. P.O. Box 73 Lexington, MA 02173-0073		10. PROGRAM ELEMENT, PROJECT, TASK AREA & WORK UNIT NUMBERS Program Element No. 63250F Project No. 649L
11. CONTROLLING OFFICE NAME AND ADDRESS Air Force Systems Command, USAF Andrews AFB Washington, DC 20331		12. REPORT DATE 15 August 1985
		13. NUMBER OF PAGES 68
14. MONITORING AGENCY NAME & ADDRESS (if different from Controlling Office) Electronic Systems Division Hanscom AFB, MA 01731		15. SECURITY CLASS. (of this Report) Unclassified
		15a. DECLASSIFICATION DOWNGRADING SCHEDULE
16. DISTRIBUTION STATEMENT (of this Report) Approved for public release; distribution unlimited.		
17. DISTRIBUTION STATEMENT (of the abstract entered in Block 20, if different from Report)		
18. SUPPLEMENTARY NOTES None		
19. KEY WORDS (Continue on reverse side if necessary and identify by block number)		
solid state devices	photodiodes	electro-optic devices
quantum electronics	lasers	charge-coupled devices
materials research	laser spectroscopy	acoustoelectric devices
microelectronics	crystal growth	microwave semiconductor devices
analog device technology	signal processing	superconductive devices
20. ABSTRACT (Continue on reverse side if necessary and identify by block number)		
<p>This report covers in detail the solid state research work of the Solid State Division at Lincoln Laboratory for the period 1 May through 31 July 1985. The topics covered are Solid State Device Research, Quantum Electronics, Materials Research, Microelectronics, and Analog Device Technology. Funding is primarily provided by the Air Force, with additional support provided by the Army, DARPA, Navy, SDIO, NASA, and DOE.</p>		

UNCLASSIFIED

SECURITY CLASSIFICATION OF THIS PAGE (When Data Entered)